

**IDENTIFICATION AND INVESTIGATIONS OF
UNTRIGGERED MAGNETAR BURSTS
IN THE FERMI GAMMA-RAY BURST MONITOR DATABASE**

by
METE UZUNER

Submitted to the Graduate School of Engineering and Natural Sciences
in partial fulfilment of the requirements for the degree of
Master of Science

Sabanci University
July 2022

METE UZUNER 2022 ©

All Rights Reserved

ABSTRACT

IDENTIFICATION AND INVESTIGATIONS OF UNTRIGGERED MAGNETAR BURSTS IN THE FERMI GAMMA-RAY BURST MONITOR DATABASE

METE UZUNER

PHYSICS M.Sc. THESIS, JULY 2022

Thesis Supervisor: Prof. Dr. Ersin Göğüş

Thesis Co-Supervisor: Assoc. Prof. Dr. Yuki Kaneko

Keywords: Magnetars, Spectral Analysis

Magnetars are isolated neutron stars with extremely high magnetic fields that are known to emit short bursts. In this thesis, short bursts from two magnetars, *Swift* J1818.0-1607 and PSR J1846.4-0258 (a rotation-powered pulsar), which were burst active during 2020 and early 2021 were investigated, using *Fermi* Gamma-ray Burst Monitor (GBM) data.

Firstly, candidate events were identified among the blind search results with GBM data, based on positive correlation between the count rates and cosine of the angles between the detectors' zenith to a specific source. Then, we filtered events with non-positive correlation out of our event sample by considering that they were not originated from *Swift* J1818.0-1607 or PSR J1846.4-0258. We identified 115 bursts likely coming from these sources in total. Moreover, we performed spectral analysis for all spectra in 8-200 keV energy range and at 8 ms resolution using Comptonized (COMPT), single black body (BB), and sum of two black body models (BB+BB).

We found that the identified bursts in our sample have relatively shorter duration in comparison to the other magnetar bursts in literature. Moreover, these bursts can be modeled well by BB. For both sources, we found similar BB temperatures as $kT \sim 10 - 11$ keV. Also, we found that there is a negative correlation between kT and the emission area as reported in other magnetar studies.

ÖZET

TETİKLEMEMİŞ MAGNETAR PATLAMALARININ FERMİ GAMA-IŞINI İZLEME MONİTÖRÜ VERİTABANI KULLANILARAK ARAŞTIRILMASI VE İNCELENMESİ

METE UZUNER

FİZİK YÜKSEK LİSANS TEZİ, TEMMUZ 2022

Tez Danışmanı: Prof. Dr. Ersin Göğüş

Eş Tez Danışmanı: Doç. Dr. Yuki Kaneko

Anahtar Kelimeler: Magnetarlar, Tayfsal Analiz

Magnetarlar yüksek manyetik alanlara sahip, kısa patlamalar yapan izole nötron yıldızlarıdır. Bu tez çalışmasında, Fermi Gamma Işını Uzay Teleskobu (Fermi) üzerindeki Gamma Işını Gözlem Monitörü (GBM) kullanılarak, 2020’de ve 2021 yılının ilk kısmında aktif olduğu bilinen *Swift* J1818.0-1607 ve PSR J1846.4-0258’den gelen kısa patlamalar incelendi.

İlk olarak, aday patlamalar, dedektör eksenini ve kaynak arasında kalan açı dedektörünün topladığı foton oranıyla karşılaştırılarak ve bu karşılaştırma sırasında pozitif korelasyon elde edilip edilmediği kontrol edilerek belirlendi. Pozitif korelasyon elde edilmeyen patlamalar, bu patlamaların *Swift* J1818.0-1607 veya PSR J1846.4-0258 kaynaklı olmadığı düşünülerek elendi. Bu iki kaynaktan gelen toplam 115 patlama tespit ettik. Daha sonra 8-200 keV enerji aralığında, 8 ms çözünürlükte Compton, kara cisim, ve kara cisim + kara cisim tayfsal modelleri kullanılarak tüm patlamalar için tayfsal analiz yaptık.

Tespit ettiğimiz patlamaların literatürdeki diğer magnetar patlamalarına göre daha kısa olduğunu bulduk. Buna ek olarak, iki kaynağın tayfının da kara cisim modeline uyumlu olduğunu bulduk. İki kaynak içinde benzer kara cisim sıcaklık değerleri elde ettik ($kT \sim 10 - 11$ keV). Ayrıca, ışınma alanlarıyla kara cisim sıcaklıkları arasındaki negatif korelasyonun, diğer magnetar patlamalarıyla benzer olduğunu gözlemledik.

ACKNOWLEDGEMENTS

I would like to thank my co-advisor Yuki Kaneko and my advisor Ersin Göğüş for their support and guidance. I am thankful for their time and effort that they spent on helping me. I would also like to thank my research teammate Özge Keskin for her valuable comments.

I would like to thank my family, especially my mom Fatma Aldemir, my grandfather Cevat Arık, my grandmother Seniye Arık, and İlayda Akbulut for supporting me during my journey. Lastly, I would also like to thank my dear friends.

I acknowledge support from the Scientific and Technological Research Council of Turkey (TÜBİTAK) BİDEB 2210E program. I also acknowledge support from TÜBİTAK project (grant no: 118F344).

To my grandparents

TABLE OF CONTENTS

LIST OF TABLES	ix
LIST OF FIGURES	x
1. INTRODUCTION	1
1.1. Fermi Gamma-Ray Space Telescope	4
2. Burst Identification	7
2.1. <i>Swift</i> J1818.0-1607	8
2.2. PSR J1846.4-0258	8
2.3. Burst Search and Identification Methods	9
3. Spectral Analysis	16
3.1. Detector Selection	16
3.2. Determination of Burst Duration	17
3.3. Energy Interval Selection	17
3.4. Spectral Model Selection.....	19
3.4.0.1. Comptonized Model (COMPT)	19
3.4.0.2. Black Body Model (BB).....	19
4. Analysis Results	21
5. Discussion	26
5.1. Future Prospects.....	33
BIBLIOGRAPHY	34

LIST OF TABLES

Table 2.1. List of <i>Swift</i> J1818.0-1607 and PSR J1846.4-0258 bursts identified with our search	12
Table 4.1. Preferred Spectral Models for <i>Swift</i> J1818.0-1607 and PSR J1846.4-0258	23
Table 4.2. List of spectral analysis results of <i>Swift</i> J1818.0-1607 events. The uncertainties are 1σ . COMPT results are shown only for the events whose spectra are better described with COMPT than BB. ...	23
Table 4.3. List of spectral analysis results of PSR J1846.4-0258 events. The uncertainties are 1σ . COMPT results are shown only for the events whose spectra are better described with COMPT than BB. ...	24

LIST OF FIGURES

Figure 1.1. 30 magnetars (16 SGRs and 14 AXPs) in the McGill Magnetar Catalog (Olausen & Kaspi, 2014). This figure is in equatorial coordinate system. Each colorful point represents a different magnetar, and the grey line represents the galactic plane. Concentrated distribution of magnetars around galactic plane is clearly seen in the figure.	2
Figure 1.2. Location of detectors on Fermi in schematic figure (left) and picture (right) is shown here. BGO detectors (b0 & b1) are located on opposite sides of GBM, and 12 NaI(Tl) detectors (n0 to nb) are located on the four edges of GBM (Bissaldi et al., 2009).	5
Figure 2.1. Nearby SGR sources to <i>Swift</i> J1818.0-1607 and PSR J1846.4-0258 are represented.	7
Figure 2.2. Table shows the events from four sources which were active in 2020 and January 2021. showing SGR J1935+2154 and SGR J1830-0645 events were also taken by papers in preparation (Lin et al. 2020, Lin et al. in prep, Roberts et al. in prep). Dashed lines represent bursts detected with Swift/BAT, green shaded areas represent our search period for <i>Swift</i> J1818.0-1607 and PSR J1846.4-0258. (Ambrosi et al. (2020) & Malacaria & Fermi GBM Team (2020)). (References: Evans et al. (2020), Bernardini et al. (2020), Barthelmy et al. (2020), Gronwall et al. (2020))	10
Figure 2.3. Angle for each detector are calculated for the location of <i>Swift</i> J1818.0-1607 for the bursts on 2020-02-03 17:52:15.577 UTC (left), and for the burst on 2021-01-06 22:22:35.771 UTC (right). Linear regression results with positive slope of 1.054 ± 0.337 (left), and non-positive slope of -0.044 ± 0.158 (right). We conclude that the burst on left is likely coming from <i>Swift</i> J1818.0-1607, but the burst on right originates from another source.	11

Figure 2.4. An example burst on 2020-04-27 18:26:20.136 UTC. Light curve of 12 NaI detectors is shown in left, and the fit result is shown in the right. The detector with the third lowest degree (n_0) was blocked at the trigger time. Therefore, the detector detects significantly lower count rates, which causes deviation from the linear fit (right).	12
Figure 2.5. Localization result for <i>Swift</i> J1818.0-1607. Diamond data points show nearby SGR sources. Data points in green, yellow, and red colors represent likely, less likely, and unlikely bursts which are coming from <i>Swift</i> J1818.0-1607, respectively.	14
Figure 2.6. Localization result for PSR J1846.4-0258. Diamond data points show nearby SGR sources. Data points in green, yellow, and red colors represent likely, less likely, and unlikely bursts which are coming from PSR J1846.4-0258, respectively.	15
Figure 2.7. Fermi/GBM light curve of 18 July 2020 between 8 to 9 hours. We identified several bursts from PSR J1846.4-0258, as labeled with the name in Table 2.1. The figure was produced by combining 16-ms binned TTE data of the two brightest detectors (NaI 10&11) in 10-100 keV energy range.	15
Figure 3.1. Light curve shows combined data of NaI 3&5 for the burst on 2020-12-13 03:53:30.677 UTC (S42). Vertical white lines represents the beginning and ending time of the Bayesian block during the burst. Horizontal red lines before and after the burst show the background block, and white horizontal line shows 1σ above the background. . . .	17
Figure 3.2. In the left image, an example light curve with source and background selection of the third detector's data for the burst at 629524415.665 MET in RMFIT can be seen. The data is binned with 8 ms resolution. Vertical dotted line represent the data used for background modeling, and blue dotted line represent the background model. Right image is zoomed in version of the left image. Here shaded area represents the source interval (bins where the burst occurred).	18
Figure 4.1. BB+BB model fits for two spectra of PSR J1846.4-0258, P18(left) and P30(right). The colored symbols are the background-subtracted count rates for each detector, and black-dashed lines are the model count rates. Sigma residuals are shown at the bottom. . . .	21
Figure 4.2. Light curve of 12 NaI detectors for the burst at 2020-07-18 08:43:47.599 UTC (P18). This is one of the COMPT preferred events. This is also a Fermi triggered event.	22

Figure 5.1. Energy fluxes as a function of burst duration in 8–200 keV for both <i>Swift</i> J1818.0-1607 (blue circles) and PSR J1846.4-0258 (red squares). Filled data points with orange and purple color represent the triggered events.	27
Figure 5.2. Duration distributions of <i>Swift</i> J1818.0-1607 (left) and PSR J1846.4-0258 (right) bursts. Red lines represent the BB duration blocks, and blue lines represent the log-normal fit.	28
Figure 5.3. Fluence as a function of kT for both <i>Swift</i> J1818.0-1607 and PSR J1846.4-0258 events.	29
Figure 5.4. Burst cumulative fluence as a function of time for both <i>Swift</i> J1818.0-1607 (left) and PSR J1846.4-0258 (right). The first burst observed for both sources are selected as the reference time. Filled data points with orange and purple color represent the triggered events. Red dashed lines represents the least-square linear fits in different time range.	30
Figure 5.5. Emission areas vs. single BB temperatures for <i>Swift</i> J1818.0-1607 (left) and PSR J1846.4-0258 (right).	30
Figure 5.6. Histogram of BB temperature of <i>Swift</i> J1818.0-1607 and PSR J1846.4-0258 events.	31
Figure 5.7. BB temperature as a function of time of <i>Swift</i> J1818.0-1607 (left) and PSR J1846.4-0258 events (right). Filled data points with orange and purple color represent the triggered events.	32

1. INTRODUCTION

Neutron stars are extremely dense objects; a typical mass of about $1\text{--}2\text{ }M_{\text{sun}}$ is found within a volume of about 10 km of radius. They are formed by the core collapse of evolved massive star leading to supernova explosions (Vidaña, 2018). Via inverse beta decay during the collapse phase, protons and relativistic electrons combine to form neutrons and electron neutrinos are produced.

$$(1.1) \quad p + e^- \longrightarrow n + \bar{\nu}_e$$

Their gravitational stability is achieved by outward neutron degeneracy pressure.

The outermost layer of a neutron star is the solid crust with a thickness of ~ 1 km. Density and pressure increase in deeper parts of neutron stars (Zavlin & Pavlov, 2002). Surrounding the crustal surface, there is a thin atmospheric plasma (Vidaña, 2018) that can affect radiation emerging from the neutron star (Thompson & Duncan 2001, Thompson, Lyutikov & Kulkarni 2002).

Magnetars had first been noticed in 1979 via observations of repeated energetic burst of gamma rays from SGR 0526–66 (Mazets et al., 1979). The spectral energy distribution of these bursts differed significantly from that of cosmological Gamma-Ray Bursts (GRBs), which are non-repeating gamma-ray radiation with non-thermal spectrum from random locations in the sky (Berger, 2014). In particular, those repeated bursts were dominated by lower energy gamma ray photons. For that reason, sources of these bursts were identified as Soft Gamma Repeaters (SGRs; Kouveliotou et al., 1993). Additionally in 1980, a source with unusually bright X-ray emission that was periodically modulated was detected (Gregory & Fahlman, 1980). The energy output of this system exceeded its available rotational power by orders of magnitude. For that reason, this object was termed as an Anomalous X-ray Pulsar (AXP; van Paradijs, Taam & van den Heuvel, 1995), which became the prototype for another subclass of magnetar type neutron stars. The current common consensus is that both AXPs and SGRs are magnetars but differ in their evolutionary stages (Vidaña, 2018).

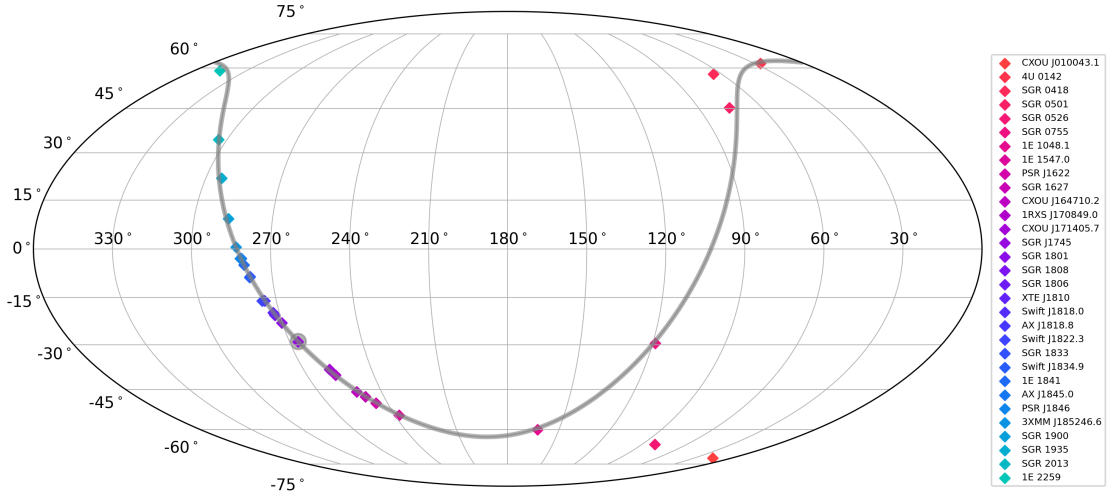


Figure 1.1 30 magnetars (16 SGRs and 14 AXPs) in the McGill Magnetar Catalog (Olausen & Kaspi, 2014). This figure is in equatorial coordinate system. Each colorful point represents a different magnetar, and the grey line represents the galactic plane. Concentrated distribution of magnetars around galactic plane is clearly seen in the figure.

Magnetars have spin periods in the range of 2-12 s, and spin-down rates of the order of 10^{-11} s/s (Esposito et al., 2009). Their X-ray luminosity is $\sim 10^{33} - 10^{36}$ erg.s $^{-1}$. Their most distinguishing property is the energetic bursts: Typical magnetar bursts lasts only 0.1-0.2 s but releases energy of $\sim 10^{39} - 10^{41}$ erg/s (Turolla, Zane & Watts, 2015). In some cases, thousands of bursts were emitted in rather short time.

Out of nearly 30 known magnetars (Olausen & Kaspi, 2014), 28 of them are in the Milky Way. Galactic magnetars are located very close to the Galactic Plane. Figure 1.1 shows the space distributions of magnetars using the data collected from the McGill Magnetar Catalog (Olausen & Kaspi, 2014). Magnetars are expected to be not much older than 10^5 year assuming they have spatial velocity of 200 ± 100 km.s $^{-1}$ (Tendulkar, Cameron & Kulkarni, 2013).

Unlike coherently radio emitting neutron stars, that is radio pulsars, rotational energy loss of magnetars is not enough to power high persistent X-ray luminosities. It can also not be attributed to the accretion mechanism because there has been no detection of any companion star. Their main source of energy is considered to be magnetic instabilities within their extreme magnetic fields, which cracks the crust of the magnetar and causes repeated soft bursts (Thompson & Duncan, 1995). This process releases large enough energy for typical SGR bursts as well as their persistent X-ray emission, but not enough for giant flares (e.g. the giant flare on 5 March 1979) (Duncan & Thompson, 1994).

Giant flares are unusually bright, sudden (rise time of a few ms), highly energetic (over 10^{44} erg.s $^{-1}$ at peak luminosity) bursts. Their duration is about a few minutes. The giant flares are preceded by a hard initial spike, followed by thermally oscillating tail emission. These events are triggered by a large scale readjustment of the stellar field. The cooling of a pair plasma trapped in the stellar magnetosphere results in hyper-Eddington, quasi-black body emission with a simple light curve and weak spectral evolution, in agreement with observations of the three giant flares to date (Duncan & Thompson, 1994).

Magnetars also exhibit X-ray outbursts, which is the sudden enhancement of the emitted flux by orders of magnitude (Rea & Esposito, 2011). Magnetar outbursts last much longer than bursts, from a few weeks to months (Kaspi & Beloborodov, 2017).

No radio emission was detected from magnetars until 2000s although radio emission from weakly magnetic neutron stars had been observed. First discovered radio-loud magnetar was XTE J1810-197 (Camilo et al., 2006). Radio emission from this source was detected after X-ray outburst in 2003. Currently, only five magnetars was detected in radio, which makes harder to find new magnetars because they are detected only by emission in high energies in most cases (Rajwade et al., 2022).

In this thesis, we aimed to identify and investigate untriggered bursts from two gamma-ray sources, *Swift* J1818.0-1607 (magnetar) and PSR J1846.4-0258 (Rotation-Powered Pulsar, RPP) in 2020-21. Activation of both sources was confirmed with triggered events detected by Gamma-ray Bursts Monitor (GBM) on the Fermi Gamma-ray Space Telescope (Fermi) and Burst Alert Telescope (BAT) on the Neil Gehrels Swift Observatory (Swift) in 2020 and early 2021. By spectral investigations of identified bursts, we aimed to clarify what distinguishes magnetars from RPPs, which has been unclear problem in neutron star physics after emission of short magnetar-like bursts from PSR J1846.4-0258 in 2006 (Gavril et al., 2008). In this thesis, only Fermi data were used. Fermi and data types shared by Fermi team are introduced in Section 1.1. Chapter 2 presents our methods to search for untriggered bursts and how we decided which bursts were originated from *Swift* J1818.0-1607 or PSR J1846.4-0258. We searched for a positive correlation between count rates and cosine of detector-to-source angle, and we identified 54 bursts from *Swift* J1818.0-1607 and 61 bursts from PSR J1846.4-0258. In Chapter 3, we describe how spectral analysis was performed for 115 bursts observed with Gamma-Ray Bursts Monitor (GBM) on Fermi. Chapter 4 presents best-fitted spectral parameters, burst duration, burst fluences, and discussion on our results. We found that all 115 spectra can be modeled with

single black body, and only two events, both from PSR J1846.4-0258, have higher energy component.

1.1 Fermi Gamma-Ray Space Telescope

Fermi is a space observatory, launched by NASA in June 2008. Fermi's scientific aim is to observe gamma ray emitting objects and transient gamma ray events, including Gamma-Ray Bursts (GRBs) with energies higher than 10 keV. Fermi carries two science instruments, which are the Large Area Telescope (LAT) and the Gamma-ray Burst Monitor (GBM). Both instruments have capabilities to work on different energy ranges. LAT can observe gamma-rays with energies between ~ 20 MeV to ~ 300 GeV (?), and GBM can observe gamma-rays with energies between ~ 8 keV to ~ 40 MeV (Meegan et al., 2009).

GBM carries 14 scintillation detectors, 12 of them are thallium activated sodium iodide scintillation detectors (NaI(Tl)) which make observation between 8 keV to 1 MeV energy range, and two of them are bismuth germanate detectors (BGO) which make observation between 200 keV to 40 MeV. 12 NaI detectors are located on GBM so that positions of bursts can be estimated by comparing count rates between each detectors ($\sim 5^\circ$ resolution) (Meegan et al., 2009). GBM detectors can find bursts in whole unocculted sky (all-sky monitoring). When a burst is detected by GBM, Fermi orients itself to let LAT observations of the burst region.

For the GBM to be triggered, at least two of NaI detectors are required to detect signals above the threshold. The threshold is determined by background level (last 17 seconds except the nearest 4 seconds) (Meegan et al., 2009). If GBM is triggered, it cannot be triggered for the following 300 seconds due to triggering algorithm even if the source is inside the field of view. This triggering setting reinforces the importance of untriggered event search inside whole data.

GBM can also detect other gamma-ray sources like Solar Flares (SF) or Terrestrial Gamma-ray Flashes (TGF). Therefore, triggering algorithm of GBM is divided into four different energy ranges: 25-50 keV for SGRs and soft GRBs, >100 keV for GRBs, >300 keV for hard GRBs and TGFs, and 50-300 keV similar to the Burst and Transient Source Experiment (BATSE), which was an instrument located on the Compton Gamma-Ray Observatory in Earth's orbit to observe GRBs.

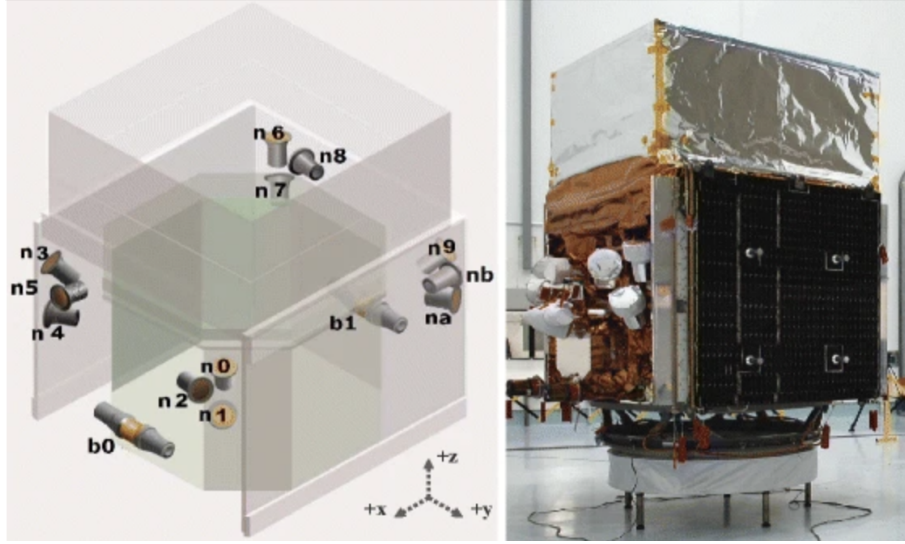


Figure 1.2 Location of detectors on Fermi in schematic figure (left) and picture (right) is shown here. BGO detectors (b0 & b1) are located on opposite sides of GBM, and 12 NaI(Tl) detectors (n0 to nb) are located on the four edges of GBM (Bissaldi et al., 2009).

Data processing unit on GBM produces three types of data, called CTIME (continuous high time resolution), CSPEC (continuous high spectral resolution), and TTE (time tagged events during triggered events). After July 2010, TTE data, which had been saved only during bursts before, was started to save as continuously (CTTE). CTIME and CSPEC data exist as pre-binned data (64 ms and 1.024 ms respectively) for each day, and TTE data exist as unbinned data ($2 \mu\text{s}$ resolution) for each hour. CTIME data has 8 energy channels, and CSPEC and TTE data have 128 energy channels over the whole duration of data. CTIME, CSPEC, and TTE data have also metadata which keep information like observation time, energy range, and time range.

To make a comparison between theoretical and observational count spectrum, Response Files (RSP) are used. An RSP file is valid to use only for a specific detector, specific coordinates on the sky, and specific time. For this reason, RSP files are required for each detector used in spectral analysis. GBM team shares RSP files for each triggered events created for the trigger time of the burst. For untriggered transient events, researchers need to use GBMRSPGEN, which is a tool to create RSP files for any specific time, to create RSP files.

Detector Response Matrix (DRM) is a two dimensional matrix (photon bins vs. number of channels) which converts photon spectrum into count rate spectrum to be used while performing spectral analysis (Kaneko, 2005). Effective area of detectors depends on angle between source and detector's zenith. Due to this angular dependency, GBM team shares response files with multiple DRMs, named with '.rsp2'

extension for triggered events. Multiple DRMs are generally required to study spectrum of long bursts ($\gtrsim 100$ s) to consider effects due to the motion of the spacecraft within the burst duration. Spectral analysis of short bursts can be performed with a single DRM because spacecraft will not move much in short times.

2. Burst Identification

GBM can detect a burst if the burst signals are above the trigger threshold, which is $\sim 0.7 \text{ photons cm}^{-2} \text{ s}^{-1}$ in 50-300 keV range with one second peak (Meegan et al., 2009). However, many dim bursts do not have enough signal above background, and they do not trigger GBM. Therefore, we need to search untriggered bursts, which were not recognized as triggered events with GBM. In this section, we presented gamma-ray sources we investigated in this study, our burst identification method, and our burst selection method.

For this study, two gamma-ray sources, *Swift* J1818.0-1607 and PSR J1846.4-0258 (see Figure 2.1), which were active in 2020 were selected.

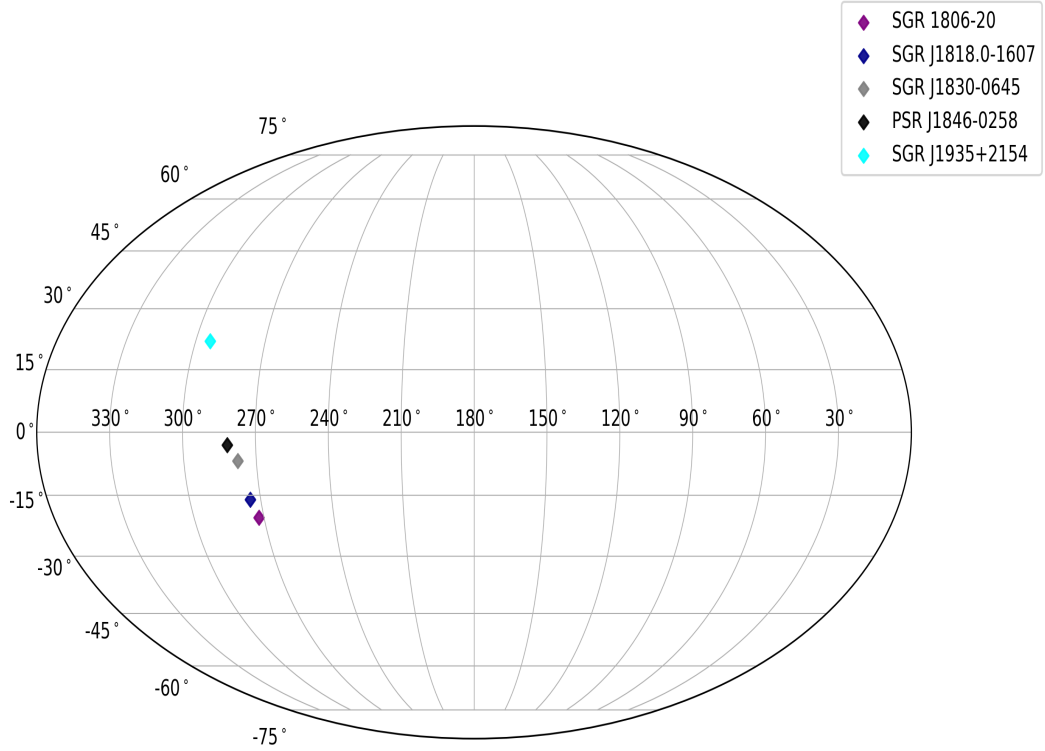


Figure 2.1 Nearby SGR sources to *Swift* J1818.0-1607 and PSR J1846.4-0258 are represented.

2.1 *Swift* J1818.0-1607

Swift J1818.0-1607 was discovered on 12 March 2020 by Swift/BAT observation of the x-ray outburst (Evans et al., 2020). Its spin period has been found as 1.36 sec (Enoto et al., 2020). It could be the one of the youngest magnetar with characteristic age ($\tau = P/2\dot{P}$) of ~ 500 years (Champion et al., 2020). *Swift* J1818.0-1607 is also the fifth radio-loud magnetar discovered until now (Rajwade et al., 2020).

2.2 PSR J1846.4-0258

PSR J1846.4-0258 is a young rotation powered x-ray pulsar, located in the center of a young shell-type supernova remnant called Kes 75 (known as G29.7-0.3). Its spin period is 326 ms, its characteristic age is $\tau_c = 723$ year, and its magnetic field is $B = 5 \times 10^{13}$ G, which makes the magnetic field of PSR J1846.4-0258 just above the quantum critical field (Gotthelf, 2000). In terms of magnetic field, PSR J1846.4-0258 has lower magnetic field than significant majority of magnetars; however, it has higher magnetic field than typical RPPs. Furthermore, PSR J1846.4-0258, which considered as an RPP with spin-down luminosity higher than x-ray luminosity, emitted magnetar-type bursts in 2006 (Gavriil et al., 2008). The detected bursts were short (< 0.1 s), brighter than Eddington luminosity (L_E) (one bursts with luminosity $> 10L_E$) with assumption of $1.4M_\odot$ neutron star with 6 kpc distance, and repeated x-ray bursts. This magnetar-type activity complicated to distinguish RPPs from magnetars. There had been no detected radio emission from PSR J1846.4-0258 during activity period in neither 2006 (Archibald et al., 2008; Livingstone et al., 2006), nor 2020 (Blumer et al., 2021). Weaker radio emission or radio emission beamed elsewhere might prevent detection in radio (Archibald et al., 2008).

2.3 Burst Search and Identification Methods

We performed blind searches for gamma-ray transient events in 2020 and early 2021, during which the two sources were burst active. A significant increase in count rates above the estimated background level with at least two detectors was considered as an event without event-type classification. To determine the significance in the count rate increase, we used three statistical methods: signal-to-noise ratio (SNR), Poisson statistics, and Bayesian block (Scargle et al. 2013), in 4 different modes with different energy ranges and resolutions. The minimum significance criteria were $>4.5\sigma$ for SNR method and $P \leq 10^{-4}$ for Poisson method. In this thesis, this event database was used to identify bursts which were originated from *Swift* J1818.0-1607 or PSR J1846.4-0258 .

Swift J1818.0-1607 triggered Swift/BAT on 12 March 2020 (Evans et al., 2020), 6 May 2020 (Barthelmy et al., 2020), 16 May 2020 (Gronwall et al., 2020), and 2 July 2020 (Bernardini et al., 2020); and triggered Fermi/GBM on 13 December 2020, 6 January 2021, and 24 January 2021. Therefore, we selected to search untriggered bursts from the beginning of February 2020 to the end of June 2020, and from the beginning of December 2020 to the end of January 2021.

On 1 August 2020, PSR J1846.4-0258 triggered Fermi/GBM and Swift/BAT (Krimm, Lien, Page, Palmer, Tohuvavohu & Neil Gehrels Swift Observatory Team, 2020). Therefore, we selected to search untriggered bursts from the beginning of July 2020 to the end of September 2020.

In Figure 2.2, we present our search periods, triggered bursts, and published bursts in literature for *Swift* J1818.0-1607, PSR J1846.4-0258, as well as for SGR J1830-0645, and SGR J1935+2154, which are nearby and were active episodically in 2020 and 2021.

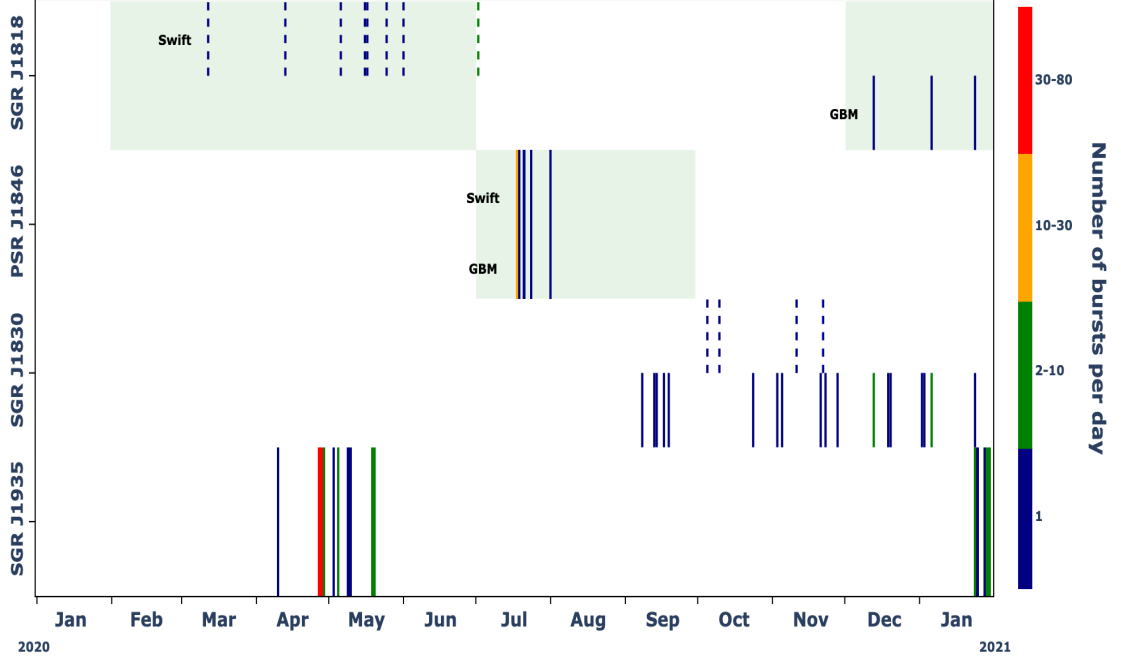


Figure 2.2 Table shows the events from four sources which were active in 2020 and January 2021. showing SGR J1935+2154 and SGR J1830–0645 events were also taken by papers in preparation (Lin et al. 2020, Lin et al. in prep, Roberts et al. in prep). Dashed lines represent bursts detected with Swift/BAT, green shaded areas represent our search period for *Swift* J1818.0-1607 and PSR J1846.4-0258. (Ambrosi et al. (2020) & Malacaria & Fermi GBM Team (2020)). (References: Evans et al. (2020), Bernardini et al. (2020), Barthelmy et al. (2020), Gronwall et al. (2020))

As an addition to Figure 2.2, one burst from SGR 1806–20 was also detected on 30 April 2020 (Ambrosi et al., 2020); however, SGR 1806–20 was not included into Figure 2.2 due to no activity during our search period except this single burst.

SGR bursts last usually less than a second and spectrally soft. Therefore, SGR bursts were searched in the database produced in 10-100 keV energy range and 8 ms resolution. Identified events by aforementioned methods could include false triggers due to Fermi’s passage through South Atlantic Anomaly (SAA) region, and events which are categorized as non-SGR events published in the Fermi Trigger Catalog¹. We determined those events in our event list by checking their burst times, then we filtered them out of our list. We also used the probability information based on the duration and hardness ratio and kept the events that are most likely SGRs. Then, we run our identification code to remaining events.

The identification of bursts among the all remaining events was based on the angle between the source and the detectors’ zenith. Because higher count rates are ex-

¹<https://heasarc.gsfc.nasa.gov/FTP/fermi/data/tdat/heasarc-fermigtrig.tdat>

pected for detectors which have closer angle to the source, we searched for a positive trend in the linear regression between the cosine of the angle and the logarithm of the peak count rates collected by the detectors. For each identified untriggered burst, NaI detectors with the highest count rates with $\leq 90^\circ$ detector-to-source angle and remaining NaI detectors with $\leq 60^\circ$ detector-to-source angle were used for each burst. We first tested this approach with events with bursts from a few known SGR sources. If the slope of the fit for a burst was non-positive (i.e., slope + $1\text{-}\sigma$ uncertainty < 0), then we considered that the burst was coming from another transient source and we removed the burst from our list (see example fit results in Figure 2.3).

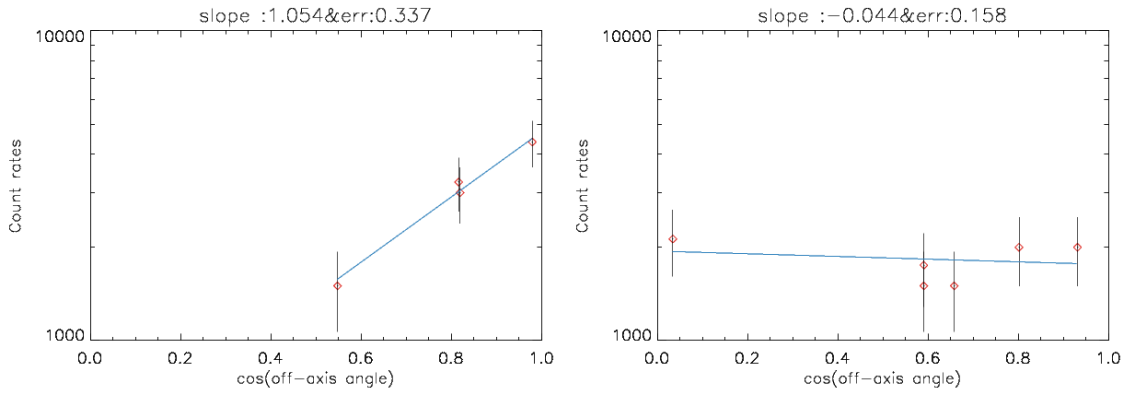


Figure 2.3 Angle for each detector are calculated for the location of *Swift* J1818.0-1607 for the bursts on 2020-02-03 17:52:15.577 UTC (left), and for the burst on 2021-01-06 22:22:35.771 UTC (right). Linear regression results with positive slope of 1.054 ± 0.337 (left), and non-positive slope of -0.044 ± 0.158 (right). We conclude that the burst on left is likely coming from *Swift* J1818.0-1607, but the burst on right originates from another source.

If any of the detector is blocked by any instruments on Fermi at the trigger time, count rates may significantly affected (see an example light curve in Figure 2.4). Therefore, we checked whether any detectors were blocked partially or fully at the trigger time via using GBMBLOCK software provided by GBM team.

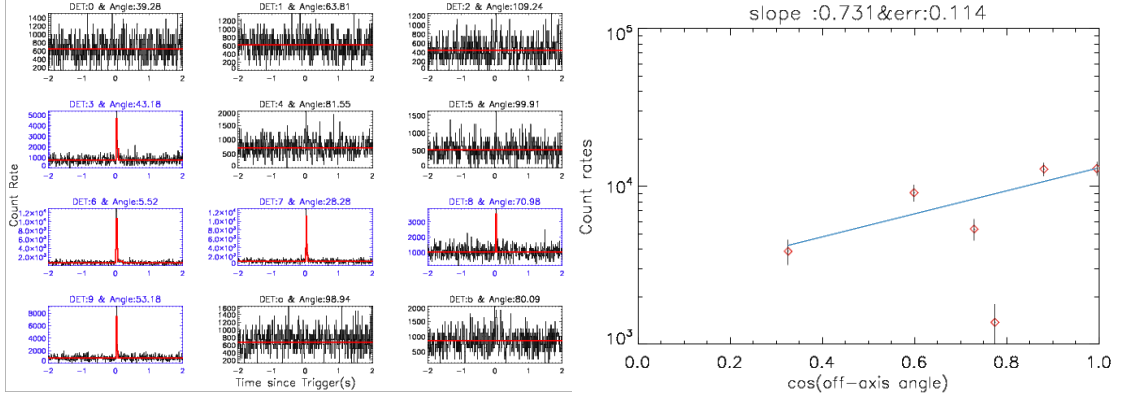


Figure 2.4 An example burst on 2020-04-27 18:26:20.136 UTC. Light curve of 12 NaI detectors is shown in left, and the fit result is shown in the right. The detector with the third lowest degree (n_0) was blocked at the trigger time. Therefore, the detector detects significantly lower count rates, which causes deviation from the linear fit (right).

All identified bursts which are likely originating from *Swift* J1818.0-1607 and PSR J1846.4-0258 based on our positive correlation results are presented in Table 2.1. We also present the Fermi/GBM light curve for the most burst-crowded hour in our search period in Figure 2.7.

Table 2.1 List of *Swift* J1818.0-1607 and PSR J1846.4-0258 bursts identified with our search

ID	Event Time (UTC) (YYMMDD hh:mm:ss)	Time (Fermi MET) (s)	Detectors ^a	Duration (ms)	Search Method ^b	SNR ^c
<i>Swift</i> J1818.0-1607						
S1 ^{TF}	200203 03:17:11.908	602392636.908	0,1,2,3,5	66	1	15.8
S2	200203 17:52:15.575	602445140.576	0,1,2,5	8	1,2,3	12.2
S3	200204 09:02:40.353	602499765.353	2,5	8 ^d	3	5.7
S4	200213 02:56:04.468	603255369.469	0,1,3,5	8	1	9.7
S5	200214 06:35:39.376	603354944.377	4,5	14	2	7.8
S6	200215 10:10:59.453	603454264.454	0,1,2,5	8	2	6.1
S7	200222 15:26:29.970	604077994.970	0,1,3	9	2	4.7
S8	200227 09:59:12.821	604490357.821	3,4	8 ^d	2	5.4
S9	200229 18:56:16.643	604695381.644	3,4	14	1,2,3	13.4
S10	200309 13:59:01.521	605455146.521	0,1,2,9	17	3	8.3
S11 ^{TS}	200312 21:16:47.328	605740612.329	0,1,3,6,9	17	1,2,3	10.8
S12	200317 11:42:36.372	606138161.373	4,8	8 ^d	3	4.5
S13	200323 10:08:47.593	606650932.594	4,8	8 ^d	2	6.1
S14	200326 16:26:12.425	606932777.426	2,10	8 ^d	3	5.4
S15	200327 13:21:42.573	607008107.574	3,4	449	1	8.2
S16	200404 21:19:24.252	607727969.252	4,7,8	6	3	5.5
S17	200406 12:37:49.372	607869474.372	2,10	3	3	5.8
S18	200411 20:15:40.989	608328945.989	8	5	2,3	6.3
S19	200412 04:06:10.872	608357175.872	6,7	8 ^d	3	4.6
S20	200418 00:09:24.886	608861369.886	9,10	9	1	8.9
S21	200425 06:34:44.643	609489289.643	9,10	5	3	10.9
S22	200425 20:20:59.720	609538864.720	7,8	8 ^d	2	5.7
S23	200501 15:35:28.235	610040133.236	9,10,11	440	1,3	8.9
S24	200502 09:22:51.711	610104176.712	7,8	8 ^d	2	5.9
S25	200502 11:41:19.601	610112484.602	8,11	8	2	7.5
S26	200509 12:57:57.391	610721882.391	6,7,11	8 ^d	2	5.2
S27	200516 15:49:32.484	611336977.485	8,11	8 ^d	2	5.9
S28	200517 14:29:54.281	611418599.281	6,7,8	8	2	6.4
S29	200519 07:15:32.836	611565337.837	8,11	8	2	6.5
S30	200520 10:23:51.123	611663036.124	9,10,11	7	3	6.1
S31	200522 19:58:13.477	611870298.478	6,7,9	5	2	6.0
S32	200523 08:32:33.465	611915558.465	6,7,9,10,11	5	1	4.6

Table 2.1 – *continued*

ID	Event Time (UTC) (YYMMDD hh:mm:ss)	Time (Fermi MET) (s)	Detectors ^a	Duration (ms)	Search Method ^b	SNR ^c
S33	200526 19:17:48.757	612213473.758	9,10,11	45	2	4.3
S34	200527 11:59:42.267	612273587.267	9,10,11	9	2,3	10.1
S35	200601 03:32:30.056	612675155.056	8,11	8	3	6.4
S36	200606 13:35:26.048	613143331.048	8,11	9	3	6.1
S37	200616 19:08:30.751	614027315.752	7,8,11	8	3	5.9
S38	200623 10:00:45.970	614599250.971	7,11	6	2	6.4
S39	200625 16:01:32.086	614793697.086	7,9,11	9	2	6.8
S40	200627 23:51:48.891	614994713.892	6,7,8,9,10,11	221	1	10.1
S41	201212 02:33:34.061	629433219.062	1,3,5	10	2	6.0
S42	201213 03:53:30.676	629524415.677	0,1,3,4,5	14	1,2,3	29.8
S43	201213 10:39:36.284	629548781.285	4,5	43	1	10.5
S44	201213 18:31:58.123	629577123.124	1,2,5	81	1,2,3	24.4
S45	201213 23:06:34.604	629593599.604	0,1,3,4,5	5	3	7.9
S46	201214 02:00:15.571	629604020.572	3,5	7	2	3.7
S47	201214 22:14:59.164	629676904.165	4,5	5	2	6.0
S48	210106 00:10:45.263	631584650.263	0,1,2,3,5	36	1,2,3	21.2
S49	210106 05:11:16.384	631602681.384	1,3,4,5	19	1,2,3	19.4
S50	210107 14:25:42.567	631722347.567	1,4,5	8 ^d	3	4.0
S51	210124 00:35:30.443	633141335.443	2,5	84	1,2,3	20.0
S52	210124 19:13:48.229	633208433.230	0,1,5	10	3	5.9
S53	210124 20:48:23.943	633214108.943	0,1,3,4	40	1,2,3	22.2
S54	210125 09:58:32.654	633261517.654	4,5	24	1,2,3	7.4
PSR J1846.4-0258						
P1	200706 11:45:28.784	615728733.786	8,11	7	3	6.5
P2	200710 04:59:48.361	616049993.361	7,11	10	2	5.9
P3	200713 05:43:39.507	616311824.507	7,8,11	12	2,3	10.4
P4	200717 17:53:31.999	616701216.999	7,8,11	10	2	6.5
P5 ^{TF}	200718 08:24:38.725	616753483.725	6,7,9,10,11	183	1,3	12.0
P6	200718 08:25:05.958	616753510.958	6,7,9,10,11	74	1,2,3	15.3
P7	200718 08:26:11.287	616753576.287	7,9,10,11	30	1,2,3	18.7
P8	200718 08:26:40.698	616753605.698	7,9,10,11	44	1,2,3	22.1
P9	200718 08:26:50.509	616753615.509	7,9,10,11	7	12	8.0
P10	200718 08:31:11.524	616753876.524	9,10,11	44	1,2,3	17.4
P11	200718 08:39:56.890	616754401.890	9,10,11	11	1,2,3	16.5
P12	200718 08:40:34.580	616754439.580	9,10,11	78	1	8.6
P13	200718 08:40:50.348	616754455.348	9,10,11	27	1,2,3	10.4
P14	200718 08:41:02.806	616754467.806	9,10,11	9	2,3	8.4
P15	200718 08:41:04.962	616754469.962	9,10,11	16	1,2,3	18.6
P16	200718 08:41:51.706	616754516.706	9,10,11	22	1,2,3	27.2
P17	200718 08:43:04.386	616754589.386	9,10,11	31	1,2,3	13.4
P18 ^{TF}	200718 08:43:47.599	616754632.599	10,11	133	1,2,3	52.5
P19	200718 08:44:04.331	616754649.331	10,11	6	1,2,3	10.9
P20	200718 08:47:54.141	616754879.141	10,11	16	1,2,3	22.6
P21	200718 08:48:51.071	616754936.071	10,11	122	1,2,3	27.1
P22	200718 09:53:58.478	616758843.478	6,7,9,10,11	14	1,2,3	9.9
P23	200718 09:56:03.452	616758968.452	6,7,9,10,11	14	1,2,3	12.7
P24	200718 10:06:41.223	616759606.223	9,10,11	25	1,2,3	13.5
P25	200718 10:07:53.283	616759678.283	9,10,11	20	2,3	9.7
P26	200718 10:11:04.196	616759869.196	9,10,11	7	1,2,3	6.9
P27	200718 11:12:11.076	616763536.076	6,7,8,9,11	5	3	11.4
P28	200718 11:39:57.349	616765202.349	9,10,11	30	1,3	9.4
P29	200718 14:35:42.363	616775747.363	6,7,9,10,11	11	1	11.6
P30 ^{TF}	200718 14:50:52.381	616776657.381	7,9,10,11	53	1,2,3	43.7
P31	200718 14:50:54.393	616776659.393	7,9,10,11	30	1,2,3	13.4
P32	200718 14:51:10.244	616776675.244	7,9,10,11	46	1,2,3	16.7
P33	200718 14:57:18.377	616777043.377	9,10,11	18	1,2,3	15.3
P34	200718 15:01:09.771	616777274.771	9,10,11	68	1,2,3	13.5
P35	200718 15:59:04.615	616780749.615	7,8,9,11	8	2,3	10.6
P36	200718 17:41:10.233	616786875.233	7,8,9,10,11	30	1	10.1
P37	200718 22:32:03.837	616804328.837	6,7,9,10,11	18	1,2,3	7.6
P38	200719 02:11:01.208	616817466.209	10,11	19	1,2,3	15.5
P39	200721 07:39:07.355	617009952.355	7,9,10,11	10	1,2,3	12.4
P40	200721 08:07:14.751	617011639.751	10,11	4	2	6.1
P41	200724 03:30:49.443	617254254.443	7,8,11	12	1,2,3	24.3
P42	200729 16:57:18.588	617734643.588	7,11	8	2	6.9
P43 ^{TF}	200801 20:11:47.639	618005512.639	9,10,11	20	1,2,3	15.8
P44	200803 16:44:44.978	618165889.978	8,11	8 ^d	2,3	6.0
P45	200804 16:24:05.600	618251050.600	9,10,11	10	3	6.5
P46	200807 05:53:41.102	618472426.102	6,7	8 ^d	2	5.5
P47	200807 22:14:11.289	618531256.289	8,11	8 ^d	3	5.9
P48	200810 16:50:33.485	618771038.485	8,11	7	2	6.8
P49	200815 15:29:09.869	619198154.869	0,9	17	2	8.0
P50	200815 16:37:19.845	619202244.845	7,8,11	6	2	7.6
P51	200818 17:58:41.728	619466326.728	7,8,11	8	2	6.1
P52	200820 17:27:43.283	619637268.283	6,7,8,11	8	2	6.6
P53	200827 04:59:46.160	620197191.160	7,8	7	3	5.7
P54	200829 04:42:23.203	620368948.203	6,7,8	8 ^d	2	5.3

Table 2.1 – <i>continued</i>						
ID	Event Time (UTC) (YYMMDD hh:mm:ss)	Time (Fermi MET) (s)	Detectors ^a	Duration (ms)	Search Method ^b	SNR ^c
P55	200908 11:52:36.389	621258761.389	6,7,8,11	9	1,2,3	7.5
P56	200913 10:53:12.824	621687197.824	6,7	8 ^d	3	5.5
P57	200914 02:40:16.384	621744021.384	6,7,8,11	12	1	17.4
P58	200917 04:06:56.137	622008421.138	3,6	10	2	7.0
P59	200917 04:08:31.609	622008516.609	0,3,6	10	3	5.3
P60	200920 02:01:12.821	622260077.821	0,3,6	3	3	5.5
P61	200927 19:48:44.762	622928929.762	3,4,7,8	8	2,3	8.0

Notes:
^{T_F} Bursts triggered GBM.
^{T_S} Bursts triggered Swift/BAT.
^a Detectors used in spectral analysis.
^b Methods by which the events are found. 1:Bayesian, 2:Poisson, 3:SN Ratio.
^c Signal to noise ratio of bursts calculated for whole duration in the energy range of 10-100 keV with two brightest detectors.
^d Duration cannot be determined by Bayesian method. Search results are used to present duration information.

In order to determine location of the events in our list, all the events were subjected to a more detailed localization algorithm developed by the GBM team (Goldstein et al., 2019; Kocevski et al., 2018). However, we note that this localization algorithm was developed to localize short GRBs below the on-board threshold, and SGR bursts in our list are much-softer. Also, this localization algorithm has large uncertainties even for bright GRB events (Goldstein et al., 2019). The localization results show that most of the events we identified are distributed around our two sources in the sky (see Figure 2.5 and 2.6). However, we have also determined some bursts from locations which have large angular separations with *Swift* J1818.0-1607 and PSR J1846.4-0258.

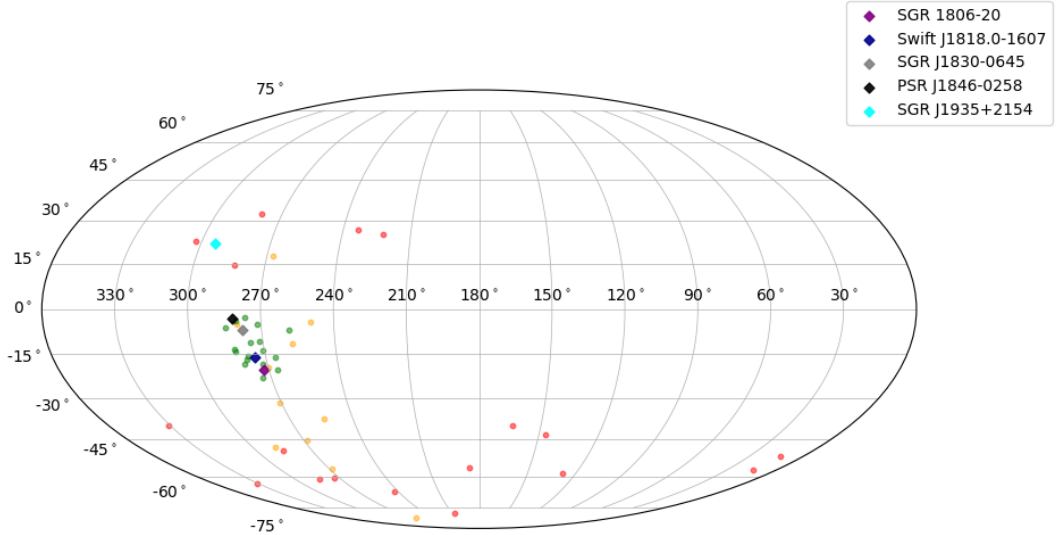


Figure 2.5 Localization result for *Swift* J1818.0-1607. Diamond data points show nearby SGR sources. Data points in green, yellow, and red colors represent likely, less likely, and unlikely bursts which are coming from *Swift* J1818.0-1607, respectively.

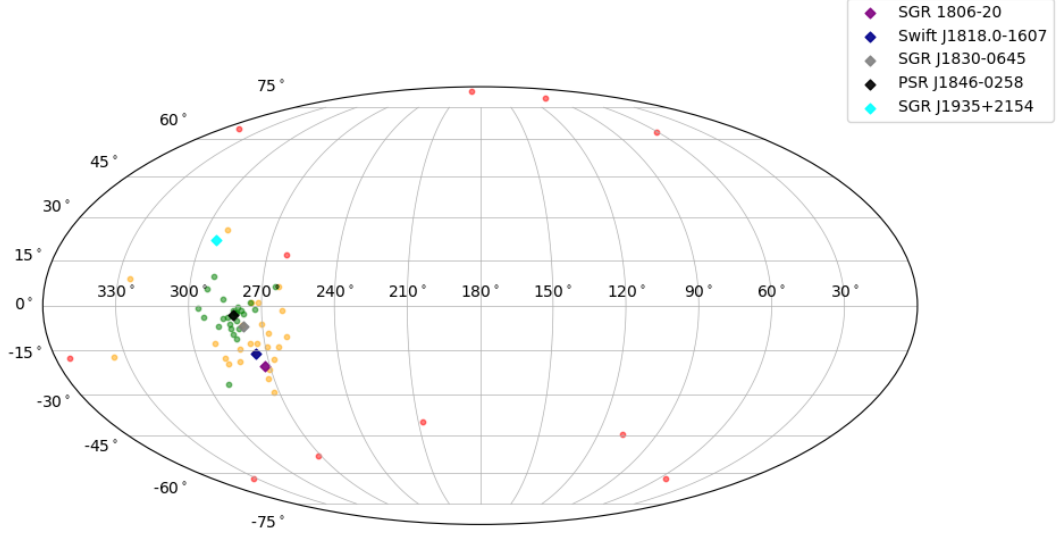


Figure 2.6 Localization result for PSR J1846.4-0258. Diamond data points show nearby SGR sources. Data points in green, yellow, and red colors represent likely, less likely, and unlikely bursts which are coming from PSR J1846.4-0258, respectively.

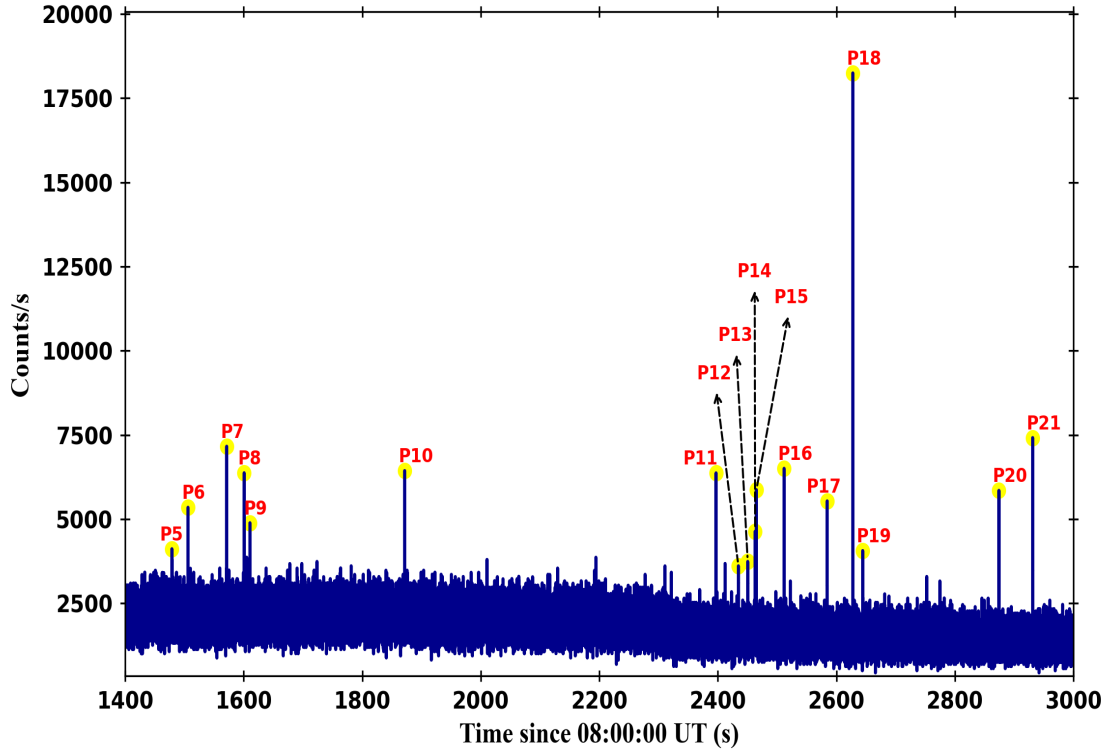


Figure 2.7 Fermi/GBM light curve of 18 July 2020 between 8 to 9 hours. We identified several bursts from PSR J1846.4-0258, as labeled with the name in Table 2.1. The figure was produced by combining 16-ms binned TTE data of the two brightest detectors (NaI 10&11) in 10-100 keV energy range.

3. Spectral Analysis

We performed time-integrated spectral analysis of all 115 bursts that we identified as *Swift* J1818.0-1607 or PSR J1846.4-0258 events, using RMFIT (version 4.3.2; Gamma-ray astronomy Group 2014). In fitting process, C-stat was used for fitting statistics, which is based on log likelihood Cash statistic (Cash, 1979). In this section, we describe the detector and time-interval selection methods as well as spectral models used in the analysis.

3.1 Detector Selection

In this study, we searched for SGR bursts, which have lower energies in comparison to GRBs. Therefore, we did not use BGO data because its energy range is much higher than typical SGR burst energies. Instead we used the data of 12 NaI detectors (8–200 keV).

We used all detectors with $<60^\circ$ to the source in spectral analysis to ensure that all detectors used in spectral analysis have the optimal viewing angles for the source. Then, we checked whether any detectors were blocked partially or fully by any instruments on Fermi at the trigger time via using GBMBLOCK software provided by GBM team. We used only unblocked detectors with $<60^\circ$ detector-to-source angle while performing spectral analysis of each spectra (see column 4 of Table 2.1).

3.2 Determination of Burst Duration

While we were performing spectral analysis, burst duration was required to select source time interval. RMFIT calculates source counts for each detector inside the selected source time interval. Firstly, we had tried to determine burst duration by running our Bayesian block algorithm on the brightest detector of each event; however, duration of bursts could not be detected for majority of bursts because they were quite dim. To prevent this, we combined data of the two brightest detectors of each burst in terms of total count rates. Then we run the Bayesian block algorithm using combined data in 1 ms resolution and 10-100 keV energy range and determined the duration of 99 (out of 115) bursts (see an example in Figure 3.1). Duration of remaining 16 bursts was determined from our blind search results in 8 ms resolution. Duration results are presented in Table 2.1.

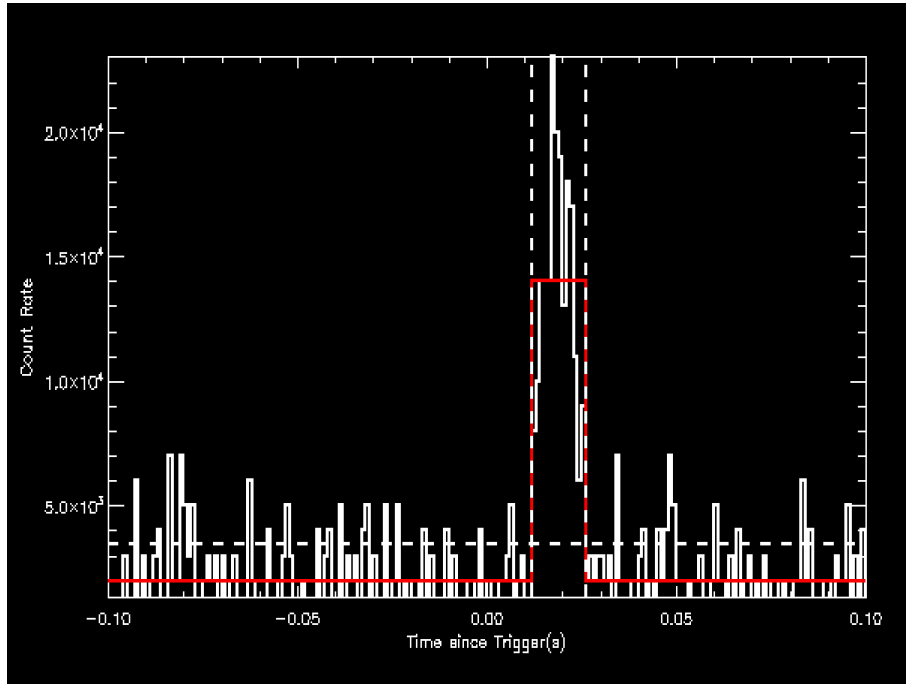


Figure 3.1 Light curve shows combined data of NaI 3&5 for the burst on 2020-12-13 03:53:30.677 UTC (S42). Vertical white lines represents the beginning and ending time of the Bayesian block during the burst. Horizontal red lines before and after the burst show the background level, and white horizontal line shows 1σ above the background.

3.3 Energy Interval Selection

SGRs emits lower energy gamma-ray photons. Since our main focus of in this study are untriggered bursts, our events are dimmer than typical triggered events. For

this reason, 8-200 keV range is chosen while performing spectral analysis. 8 keV is the sub-limit for observation of NaI detectors on GBM, and there were almost no photon but noise above 200 keV.

While performing spectral analysis, RMFIT software (version 4.3.2) was used. RMFIT determines fit parameters via forward-folding method (Gamma-ray astronomy Group, 2014). Forward-folding is a photon model dependent method which gives best fit parameter values for a selected photon model. By using a statistical test value like χ^2 , RMFIT tries to minimize difference between model count spectrum and the data collected by the telescope (Briggs, 1996).

To separate the background counts from the bursts, background counts during the selected source time should be determined. In this study, we determined background counts of each detector by using background fitting tool in RMFIT, which fits a polynomial function of the order specified by user by using the counts of each energy channel simultaneously in the user-selected background time range by minimizing χ^2 . We used first degree polynomial, and $\sim \mp 20$ s around the trigger time as background time range excluding the other bursts inside the duration and $\sim \mp 2$ s around the burst trigger time. Then, modeled background counts inside the burst duration are subtracted from the source counts. Only the background subtracted counts for each selected detectors were used for spectroscopy.

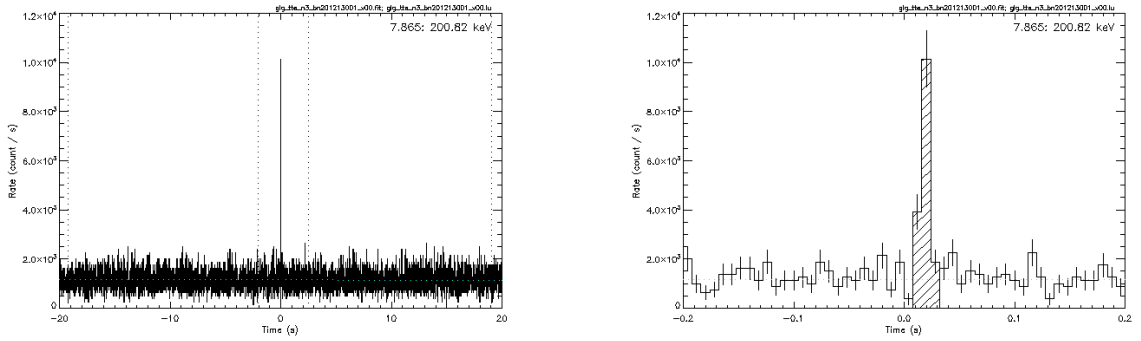


Figure 3.2 In the left image, an example light curve with source and background selection of the third detector's data for the burst at 629524415.665 MET in RMFIT can be seen. The data is binned with 8 ms resolution. Vertical dotted line represent the data used for background modeling, and blue dotted line represent the background model. Right image is zoomed in version of the left image. Here shaded area represents the source interval (bins where the burst occurred).

3.4 Spectral Model Selection

There are four frequently-used spectral models for SGR bursts; Comptonized model (COMPT) which is a power law with an exponential cut-off, single black body model (BB), double black body model (BB+BB), and optically-thin thermal bremsstrahlung model (OTTB). In this study, we fitted COMPT, BB, and BB+BB models for all events. OTTB was not included because it is essentially the same as COMPT with index = -1.

3.4.0.1 Comptonized Model (COMPT)

The first model used for SGR bursts is Comptonized model with three parameters (E_{peak} , and λ),

$$(3.1) \quad f_{\text{COMPT}} = A \exp \left[-\frac{E(2+\lambda)}{E_{\text{peak}}} \right] \left(\frac{E}{E_{\text{piv}}} \right)^{\lambda},$$

where f is the photon number flux in photons $\text{s}^{-1} \text{ cm}^{-2} \text{ keV}^{-1}$, A is amplitude in photons $\text{s}^{-1} \text{ cm}^{-2} \text{ keV}^{-1}$, E_{peak} is peak energy in keV, λ is dimensionless photon index, E_{piv} is the pivot energy used for normalization of the energy at which model is used. E_{piv} is held fixed at $\sim 100 \text{ keV}$ for GRB bursts; however, E_{piv} was used as 50 keV because SGR bursts are softer and 50 keV is closer to the middle of the energy range.

COMPT model turns into Comptonized spectrum if photon index is kept fixed at -1.

3.4.0.2 Black Body Model (BB)

The second model is BB model with two free parameters (A and kT),

$$(3.2) \quad f_{\text{BB}} = A \frac{E^2}{\exp \left(\frac{E}{kT} \right) - 1},$$

where kT is temperature in keV. BB model was also used as BB+BB models, which is the combination of the single BB model with different kT values. In BB+BB model, four free parameters (amplitudes, higher kT , and lower kT) exist. When the signal is weak (like for dim events), it becomes $kT_{\text{low}} \simeq kT_{\text{high}}$, and using second BB

model becomes unnecessary.

During our spectral investigation, we found that spectral parameters for BB+BB model was not constrained well. Therefore, we presented fit results only for BB and COMPT models.

4. Analysis Results

COMPT, BB, and BB+BB models were used in spectral analysis of all 115 spectra (54 for *Swift* J1818.0-1607 and 61 for PSR J1846.4-0258; see Table 2.1). The spectral analysis results for the bursts are presented in Tables 4.2 and 4.3.

When fitting the BB+BB model, the resulting parameters could not be constrained well for all of the events except two; generally the problem is related to low detection of higher energy photons, causing the higher kT to be not sufficiently constrained. Here, we considered kT to be well-constrained when the uncertainties are $< 30\%$ of the parameter values. The two spectra, both from PSR J1846.4-0258, that were well-fit with BB+BB have higher energy components (P18 and P30); their count spectra are presented in Figure 4.1.

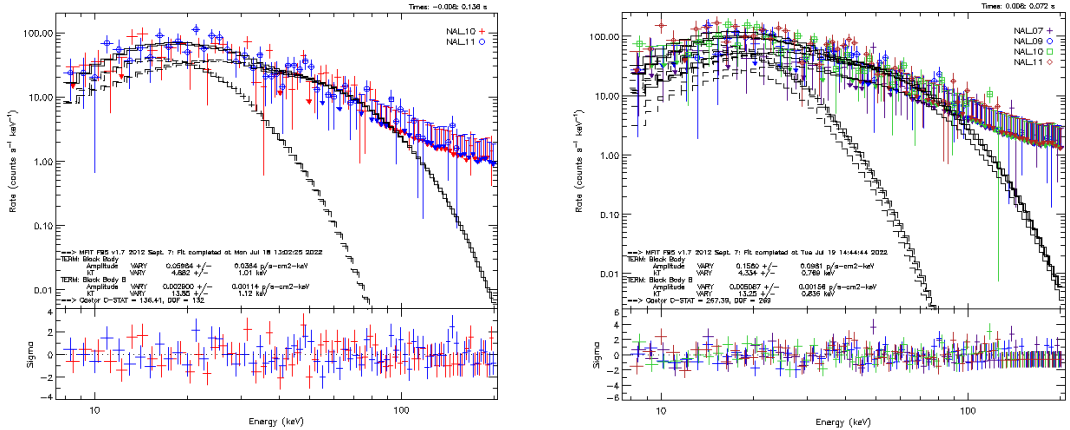


Figure 4.1 BB+BB model fits for two spectra of PSR J1846.4-0258, P18(left) and P30(right). The colored symbols are the background-subtracted count rates for each detector, and black-dashed lines are the model count rates. Sigma residuals are shown at the bottom.

Spectral parameters for the single BB model are well constrained for all events for both *Swift* J1818.0-1607 and PSR J1846.4-0258. We note that for some spectra, the lower-side uncertainties of the kT values are not constrained (i.e., $-\infty$). This happens especially when the bursts are weaker and the kT values are lower. Our data range starts from 8 keV. On the other hand, the COMPT model was able

to fit only 25% of the burst spectra statistically well. The four spectra, one of the *Swift* J1818.0-1607 spectra and three of the PSR J1846.4-0258 spectra, are relatively brighter ($\text{SNR} \geq 25$, see Figure 4.2) in comparison to all remaining spectra, and two out of these four spectra were triggered by Fermi/GBM.

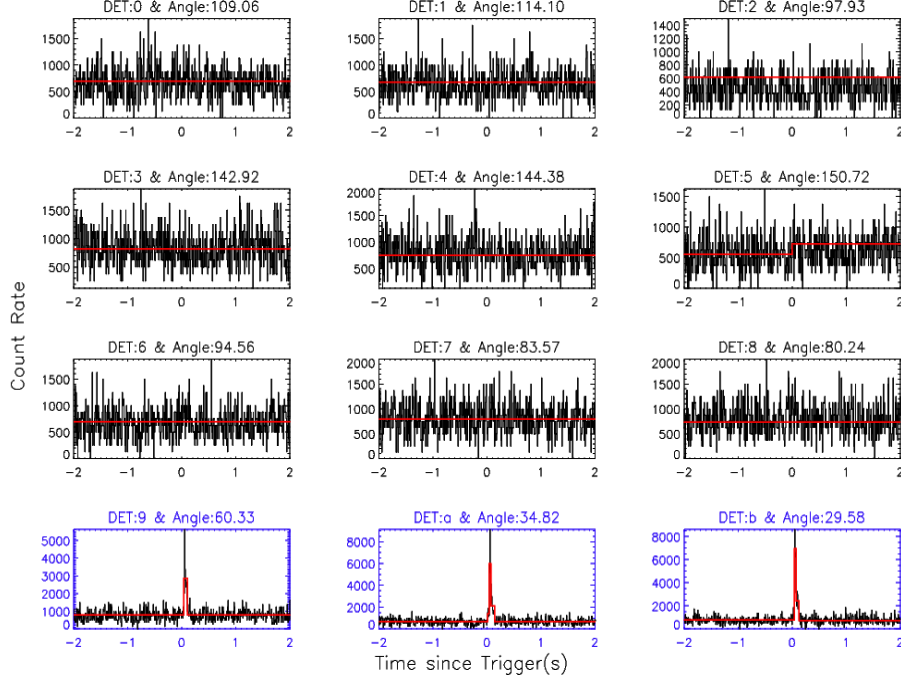


Figure 4.2 Light curve of 12 NaI detectors for the burst at 2020-07-18 08:43:47.599 UTC (P18). This is one of the COMPT preferred events. This is also a Fermi triggered event.

We used spectral fit statistics for both models to determine the best-fit model for the events which can be described with both BB and COMPT. While performing spectral fitting in RMFIT, we selected fitting statistics C-stat; however, C-stat is not a scale for goodness of fit. Therefore, we calculated Bayesian Information Criterion (BIC) (Schwarz, 1978), which is a function of C-stat value (see 4.1, to determine the best-fit spectral model.

$$(4.1) \quad \text{BIC} = -2 \ln L_{\text{max}} + k \ln N = \text{C-stat} + k \ln N,$$

where N represents how many data points exist and k represents the number of free parameters. This model evaluation method is preferable for independent and identically distributed data (Liddle, 2007). Lower BIC value means better fit with the spectral model; however, BIC difference between two models do not indicate strong preference for small differences like $|\Delta \text{BIC}| < 10$. Therefore, selection of preferred model was based on BIC differences of $|\Delta \text{BIC}| > 10$. While calculating fluences of these events, we used energy flux values of the preferred model. Statistics

for spectral analysis are presented in Table 4.1.

Table 4.1 Preferred Spectral Models for *Swift* J1818.0-1607 and PSR J1846.4-0258

Source	Number of Bursts	BB (%)	COMPT (%)
<i>Swift</i> J1818.0-1607	54	53 (98)	1 (2)
PSR J1846.4-0258	61	58 (95)	3 (5)

Table 4.2 List of spectral analysis results of *Swift* J1818.0-1607 events. The uncertainties are 1σ . COMPT results are shown only for the events whose spectra are better described with COMPT than BB.

ID	BB		COMPT			Fluence ^a (10^{-8} erg cm $^{-2}$)
	kT (keV)	C-Stat/DoF	E_{peak} (keV)	Index	C-Stat/DoF	
S1 ^{<i>T_F</i>}	11.2$^{+0.6}_{-0.6}$	375.0/338				5.62 \pm 0.40
S2	7.8 $^{+1.2}_{-1.1}$	178.7/270	30.1 \pm 6.9	-0.6 \pm 1.0	174.8/267	1.00 \pm 0.15
S3	9.5$^{+4.5}_{\text{d}}$	88.5/134				0.45 \pm 0.17
S4	5.8$^{+0.8}_{-0.7}$	238.8/269				0.62 \pm 0.08
S5	7.0$^{+2.1}_{-2.0}$	115.8/135				0.94 \pm 0.24
S6	10.0$^{+4.1}_{\text{d}}$	194.4/269				0.16 \pm 0.06
S7	18.0$^{+6.8}_{\text{d}}$	196.0/201				0.25 \pm 0.09
S8	6.7$^{+8.7}_{\text{d}}$	97.7/135				0.42 \pm 0.14
S9	7.7$^{+0.9}_{-0.8}$	112.6/135				1.64 \pm 0.24
S10	17.6 $^{+4.1}_{-3.1}$	300.3/269	71.9 \pm 17.7	0.7 \pm 1.6	300.6/268	0.74 \pm 0.19
S11 ^{<i>T_S</i>}	6.3$^{+1.0}_{-0.8}$	285.5/338				0.99 \pm 0.14
S12	5.2$^{+2.1}_{\text{d}}$	124.5/135				0.12 \pm 0.05
S13	13.8$^{+3.3}_{-2.7}$	85.0/135				0.76 \pm 0.23
S14	3.7$^{+1.5}_{\text{d}}$	109.4/133				0.15 \pm 0.05
S15	3.9$^{+0.6}_{-0.5}$	130.4/135				4.63 \pm 0.67
S16	13.3 $^{+3.1}_{-2.7}$	164.4/204	53.1 \pm 12.3	0.6 \pm 1.7	163.9/202	0.33 \pm 0.08
S17	15.6$^{+4.2}_{\text{d}}$	128.4/133				0.13 \pm 0.04
S18	19.1$^{+8.3}_{\text{d}}$	45.1/66				0.19 \pm 0.09
S19	12.3$^{+5.0}_{\text{d}}$	130.2/136				0.22 \pm 0.08
S20	8.9$^{+2.1}_{-2.0}$	132.8/133				0.61 \pm 0.13
S21	9.4$^{+1.9}_{-1.6}$	124.5/133				0.23 \pm 0.06
S22	6.7$^{+2.2}_{-2.2}$	89.9/135				0.51 \pm 0.14
S23	10.3$^{+0.9}_{-0.8}$	237.9/202				7.33 \pm 0.88
S24	6.5$^{+2.5}_{-1.6}$	82.3/135				0.45 \pm 0.14
S25	7.5$^{+2.0}_{\text{d}}$	82.1/135				0.58 \pm 0.18
S26	8.9$^{+3.1}_{-2.6}$	143.0/205				0.47 \pm 0.14
S27	11.9$^{+4.4}_{\text{d}}$	116.8/135				0.24 \pm 0.10
S28	13.5$^{+3.8}_{-2.8}$	169.2/204				0.63 \pm 0.17
S29	18.5$^{+3.8}_{-3.0}$	89.3/135				0.92 \pm 0.26
S30	7.8$^{+3.8}_{\text{d}}$	171.9/202				0.13 \pm 0.05
S31	7.3$^{+1.7}_{-1.4}$	139.1/204				0.33 \pm 0.08
S32	10.1$^{+1.8}_{-1.5}$	307.2/340				0.17 \pm 0.04
S33	15.4 $^{+3.7}_{-3.0}$	207.1/202	62.4 \pm 18.5	0.3 \pm 1.5	207.6/202	1.09 \pm 0.32
S34	11.4$^{+4.3}_{\text{d}}$	170.4/202				0.35 \pm 0.14
S35	17.9$^{+3.5}_{-2.8}$	110.0/135				0.98 \pm 0.26
S36	7.3$^{+2.1}_{\text{d}}$	104.4/135				0.30 \pm 0.10
S37	12.1$^{+4.7}_{\text{d}}$	175.4/204				0.20 \pm 0.08
S38	11.7$^{+2.3}_{-1.8}$	108.4/136				0.55 \pm 0.15

Table 4.2 – *continued*

ID	BB		COMPT			Fluence ^a (10 ⁻⁸ erg cm ⁻²)
	kT (keV)	C-Stat/DoF	E_{peak} (keV)	Index	C-Stat/DoF	
S39	14.4^{+4.5}_{-3.7}	190.8/204				0.41 ± 0.13
S40	10.3 ^{+1.1} _{-1.1}	479.0/408	40.5 ± 6.7	-0.8 ± 0.7	469.0/407	4.71 ± 0.51
S41	6.6^{+5.9}_d	171.2/201				0.10 ± 0.07
S42	7.4 ^{+0.4} _{-0.4}	352.4/338	24.4^{+3.3}_{-4.8}	-1.0^{+0.5}_d	331.3/337	2.99 ± 0.21 ^c
S43	11.6 ^{+1.6} _{-1.4}	164.4/135	50.6 ± 9.0	-0.5 ± 0.7	156.7/133	2.56 ± 0.37
S44	7.6^{+0.5}_{-0.5}	229.9/201				6.57 ± 0.47
S45	5.9^{+1.1}_{-1.0}	266.3/338				0.31 ± 0.05
S46	9.0^{+3.0}_{-3.1}	104.6/134				0.30 ± 0.10
S47	5.2^{+2.8}_d	106.4/135				0.27 ± 0.09
S48	13.0^{+0.7}_{-0.7}	322.2/337				4.23 ± 0.33
S49	9.3^{+0.6}_{-0.6}	258.3/270				3.09 ± 0.25
S50	11.5^{+2.5}_{-2.1}	154.6/202				0.39 ± 0.11
S51	6.5^{+0.6}_{-0.5}	127.0/134				11.68 ± 1.18
S52	12.2^{+3.5}_{-2.7}	167.2/201				0.47 ± 0.13
S53	9.5 ^{+0.8} _{-0.7}	370.9/270	36.0 ± 5.7	-1.1 ± 0.4	359.7/268	3.55 ± 0.32
S54	3.9^{+0.9}_{-0.6}	110.7/135				0.85 ± 0.15

Notes:^{T_F} Bursts triggered Fermi/GBM.^{T_S} Bursts triggered Swift/BAT.^a Bold entries represent the statistically preferred model.^b Fluence in 8-200 keV.^c Energy flux of Comptonized model is used.^d Negative error cannot be determined.Table 4.3 List of spectral analysis results of PSR J1846.4-0258 events. The uncertainties are 1 σ . COMPT results are shown only for the events whose spectra are better described with COMPT than BB.

ID	BB		COMPT			Fluence ^a (10 ⁻⁸ erg cm ⁻²)
	kT (keV)	C-Stat/DoF	E_{peak} (keV)	Index	C-Stat/DoF	
P1	5.4^{+1.7}_{-1.4}	92.4/135				0.42 ± 0.12
P2	12.7^{+3.0}_{-2.4}	105.6/135				0.55 ± 0.16
P3	7.1^{+0.9}_{-0.8}	160.9/203				0.89 ± 0.12
P4	6.1^{+1.7}_d	168.4/203				0.23 ± 0.07
P5 ^{T_F}	11.7^{+1.0}_{-0.9}	426.6/338				4.87 ± 0.49
P6	9.5^{+0.7}_{-0.6}	316.9/337				3.36 ± 0.30
P7	11.5 ^{+0.8} _{-0.8}	287.4/270	47.6 ± 4.6	-0.3 ± 0.5	276.9/270	2.99 ± 0.25
P8	13.5^{+0.8}_{-0.8}	286.4/270				4.44 ± 0.33
P9	8.1^{+1.3}_{-1.1}	261.1/270				0.29 ± 0.05
P10	12.3^{+1.0}_{-0.9}	215.9/202				3.49 ± 0.35
P11	13.4 ^{+1.4} _{-1.3}	203.4/202	53.9 ± 7.5	-0.2 ± 0.7	198.7/202	1.01 ± 0.13
P12	12.4^{+1.3}_{-1.2}	227.7/202				3.76 ± 0.51
P13	18.3^{+3.4}_{-3.1}	236.6/202				1.83 ± 0.32
P14	16.4 ^{+2.9} _{-2.5}	192.1/202	67.7 ± 14.9	0.2 ± 1.0	191.2/202	0.65 ± 0.14
P15	10.6 ^{+1.4} _{-1.2}	216.7/202	54.8 ± 13.5	-1.1 ± 0.6	209.9/202	1.20 ± 0.16
P16	11.2^{+0.9}_{-0.8}	208.9/202				2.15 ± 0.22
P17	10.2 ^{+1.4} _{-1.3}	211.7/202	40.4 ± 8.6	-0.9 ± 0.8	203.6/202	1.78 ± 0.24
P18 ^{T_F}	11.3 ^{+0.4} _{-0.4}	157.4/134	45.6^{+2.5}_{-2.3}	0.01^{+0.3}_{-0.3}	138.1/133	17.84 ± 0.90 ^c
P19	14.2 ^{+2.5} _{-2.2}	126.7/134	58.4 ± 10.3	0.4 ± 1.2	125.7/134	0.67 ± 0.14
P20	9.0^{+1.3}_{-1.2}	141.3/134				1.60 ± 0.24
P21	11.2 ^{+0.7} _{-0.6}	144.2/134	44.9^{+3.5}_{-3.1}	0.2^{+0.5}_{-0.4}	137.9/133	9.68 ± 0.74 ^c

Table 4.3 – *continued*

ID	BB		COMPT			Fluence ^a (10 ⁻⁸ erg cm ⁻²)
	kT (keV)	C-Stat/DoF	E_{peak} (keV)	Index	C-Stat/DoF	
P22	15.1 ^{+1.6} _{-1.4}	340.0/339	59.6 ± 6.2	0.9 ± 0.9	339.5/339	0.88 ± 0.11
P23	11.3^{+1.1}_{-1.0}	307.0/340				1.18 ± 0.14
P24	11.0 ^{+1.1} _{-1.0}	204.6/202	45.2 ± 5.9	-0.3 ± 0.7	198.9/202	2.42 ± 0.28
P25	12.3^{+1.7}_{-1.5}	197.2/202				1.46 ± 0.24
P26	12.7 ^{+1.7} _{-1.5}	188.9/202	49.8 ± 7.9	0.4 ± 1.1	188.2/202	0.74 ± 0.13
P27	9.7^{+1.5}_{-1.3}	292.0/340				0.27 ± 0.04
P28	12.4^{+1.3}_{-1.2}	197.6/202				1.76 ± 0.26
P29	14.8 ^{+1.7} _{-1.5}	309.0/339	59.1 ± 8.7	0.1 ± 0.8	307.1/339	0.84 ± 0.12
P30 ^{T_F}	10.8 ^{+0.4} _{-0.4}	296.6/270	42.5^{+2.1}_{-2.0}	-0.2^{+0.3}_{-0.3}	269.7/270	10.44 ± 0.48 ^c
P31	15.4 ^{+1.2} _{-1.1}	270.4/270	61.6 ± 5.7	0.5 ± 0.6	269.2/270	2.90 ± 0.30
P32	12.4^{+0.9}_{-0.9}	279.0/270				3.65 ± 0.34
P33	10.3 ^{+0.9} _{-0.9}	188.9/202	39.3 ± 5.0	-0.4 ± 0.6	181.6/202	1.58 ± 0.16
P34	13.2^{+1.9}_{-1.7}	263.3/202				3.37 ± 0.45
P35	10.7^{+3.6}_{-3.4}	228.2/271				0.43 ± 0.10
P36	13.4^{+1.3}_{-1.2}	339.8/338				2.32 ± 0.29
P37	13.2 ^{+1.6} _{-1.4}	326.7/339	53.6 ± 9.4	-0.3 ± 0.8	323.9/339	1.30 ± 0.18
P38	11.7^{+1.4}_{-1.3}	108.2/134				2.01 ± 0.32
P39	12.6 ^{+1.2} _{-1.1}	258.5/270	52.0 ± 6.1	0.1 ± 0.7	256.1/270	1.45 ± 0.17
P40	11.3^{+2.5}_d	94.1/134				0.16 ± 0.05
P41	10.6 ^{+0.9} _{-0.9}	183.4/203	41.2 ± 4.8	0.0 ± 0.8	179.2/203	1.98 ± 0.23
P42	9.2^{+2.4}_{-1.9}	91.8/135				0.67 ± 0.18
P43 ^{T_F}	12.2 ^{+1.2} _{-1.1}	246.5/202	54.7 ± 8.6	-0.7 ± 0.5	238.6/202	2.20 ± 0.26
P44	9.7^{+3.0}_{-2.7}	84.7/135				0.53 ± 0.18
P45	8.6^{+4.2}_d	178.4/202				0.34 ± 0.11
P46	8.5^{+2.2}_{-1.9}	80.9/135				0.51 ± 0.15
P47	12.5^{+3.0}_{-2.5}	94.4/135				0.81 ± 0.27
P48	12.0^{+3.0}_{-2.4}	104.2/135				0.62 ± 0.18
P49	7.8^{+2.0}_{-1.5}	114.7/134				0.65 ± 0.17
P50	9.5 ^{+1.9} _{-1.6}	171.9/203	39.6 ± 8.9	-0.3 ± 1.3	170.4/203	0.42 ± 0.08
P51	10.3^{+2.9}_{-3.8}	142.4/203				0.63 ± 0.18
P52	7.7^{+1.6}_{-1.6}	185.0/272				0.30 ± 0.08
P53	10.1^{+2.6}_{-2.3}	117.7/134				0.26 ± 0.07
P54	4.3^{+1.8}_d	128.5/203				0.29 ± 0.10
P55	7.2^{+1.1}_{-1.0}	280.7/272				0.45 ± 0.06
P56	11.1^{+3.6}_{-2.5}	97.4/135				0.55 ± 0.17
P57	8.5 ^{+0.9} _{-0.8}	229.5/272	31.2 ± 4.8	-0.9 ± 0.6	219.1/272	1.64 ± 0.18
P58	11.3^{+2.3}_{-2.1}	105.5/134				0.62 ± 0.17
P59	4.4^{+6.0}_d	158.5/202				0.24 ± 0.10
P60	11.4^{+3.7}_{-2.9}	127.7/202				0.18 ± 0.06
P61	10.6^{+2.5}_{-2.2}	227.9/269				0.45 ± 0.10

Notes:^{T_F} Bursts triggered Fermi/GBM.^{T_S} Bursts triggered Swift/BAT.^a Bold entries represent the statistically preferred model.^b Fluence in 8-200 keV.^c Energy flux of Comptonized model is used.^d Negative error cannot be determined.

5. Discussion

After behaving like an ordinary High-B RPP, PSR J1846.4-0258 emitted several magnetar-type bursts in 2006 (Archibald et al., 2008). The source broke its quiescence period and became active on 2020 after 14 years (Blumer et al., 2021). Similarly, fifth radio-loud magnetar PSR J1846.4-0258, which were discovered on 2020 by Swift/BAT, also became active on 2020. In the previous chapters, we have presented our results of spectral analysis for 115 bursts which we identified as originated from *Swift* J1818.0-1607 & PSR J1846.4-0258 based on our aforementioned methods. In this chapter, we discuss our spectral results, the characteristics of *Swift* J1818.0-1607 & PSR J1846.4-0258 bursts by emphasizing their similarities and differences between each other, and also with other magnetar bursts in literature.

We first investigated the duration of the identified bursts listed in the Duration column of Table 2.1. In Figure 5.1, burst flux as a function of duration based on our Bayesian block algorithm is shown. Note that a denser area at 8 ms duration can be clearly seen. Duration of some bursts could not be determined by the method explained in Section 3.2, and duration information of those bursts were extracted from the search results. The search was performed in 8 ms resolution, which causes the accumulation at 8 ms duration. Moreover, we performed log-normal fit to duration distribution of all events for both sources (see Figure 5.2). We found mean duration of 9.99 ± 0.86 ms for *Swift* J1818.0-1607, and 14.31 ± 1.50 ms for PSR J1846.4-0258.

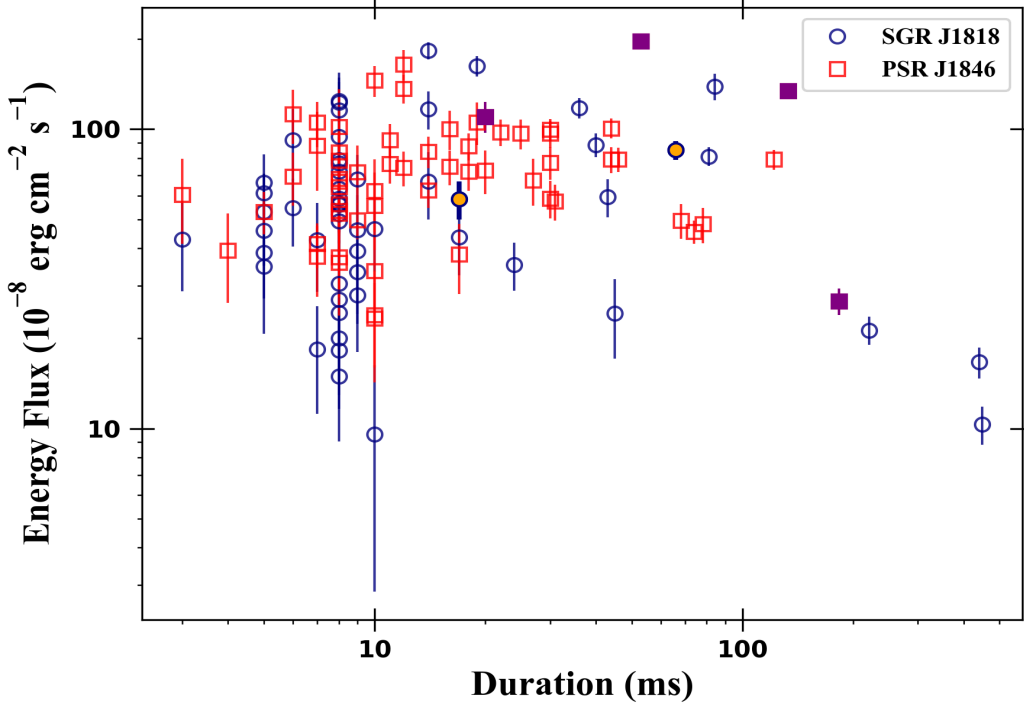


Figure 5.1 Energy fluxes as a function of burst duration in 8–200 keV for both *Swift* J1818.0-1607 (blue circles) and PSR J1846.4-0258 (red squares). Filled data points with orange and purple color represent the triggered events.

In our event sample, *Swift* J1818.0-1607 events with mean duration of 35.1 ms have comparable duration to PSR J1846.4-0258 events with mean duration of 24.9 ms. However, duration of the identified bursts in our sample have relatively shorter duration for both *Swift* J1818.0-1607 and PSR J1846.4-0258 in comparison to other reported duration of SGR events in the literature (e.g. mean duration of 169 ms for SGR J1935+2154 bursts in 2019-2020 (Lin et al., 2020), and ~ 170 ms for SGR J1550-5418 bursts in 2008-2009 (van der Horst et al. 2012, von Kienlin et al. 2012). Bursts in our list are relatively less energetic in comparison to SGR J1935+2154 and SGR J1550-5418 bursts. For a fair comparison, we compared our results with SGR J1935+2154 and SGR J1550-5418 bursts which are in the same energy flux ranges with *Swift* J1818.0-1607 and PSR J1846.4-0258. Then in common flux range, we calculated mean duration as 140.2 ms for SGR J1935+2154 bursts in 2014-2016 period (Lin et al., 2020), 302.8 ms for SGR J1935+2154 bursts in 2019-2020 period (Lin et al., 2020), and 236.2 ms for SGR J1550-5418 bursts in 2008-2009 period (von Kienlin et al., 2012). We concluded that our results are shorter about an order of magnitude in comparison to the other magnetar bursts in terms of burst duration.

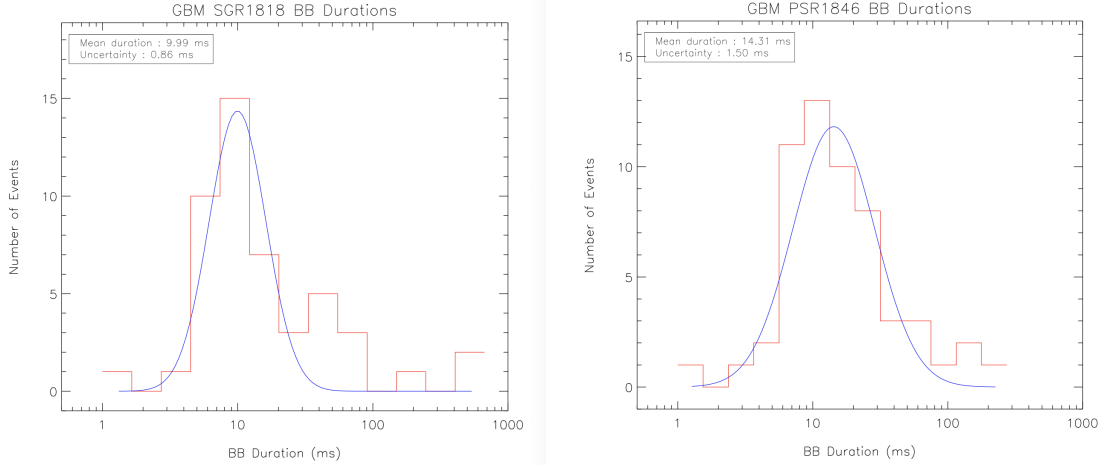


Figure 5.2 Duration distributions of *Swift* J1818.0-1607 (left) and PSR J1846.4-0258 (right) bursts. Red lines represent the BB duration blocks, and blue lines represent the log-normal fit.

The burst fluence values range in the order of 10^{-9} to 10^{-7} erg cm $^{-2}$ for both *Swift* J1818.0-1607 and PSR J1846.4-0258; we find no significant correlation between fluence and time (see Figure 5.4; Spearman's correlation coefficient, $\rho = 0.13$ & $p = 0.33$ for *Swift* J1818.0-1607 and $\rho = -0.43$ & $p = 0.0005$ for PSR J1846.4-0258). However, we found strong positive correlations for both sources ($\rho = 0.74$ & $p = 1.10 \times 10^{-10}$ for *Swift* J1818.0-1607 and $\rho = 0.90$ & $p = 5.32 \times 10^{-23}$ for PSR J1846.4-0258) between burst fluence and burst duration, which indicates flux value does not vary much.

In Figure 5.4, burst fluence as a function of BB temperature is presented. We could not find any strong correlation between fluence and kT for *Swift* J1818.0-1607 ; however, we found a weak correlation between fluence and kT for PSR J1846.4-0258 ($\rho = -0.01$ & $p = 0.92$ for *Swift* J1818.0-1607 and $\rho = 0.47$ & $p = 1.46 \times 10^{-4}$ for PSR J1846.4-0258).

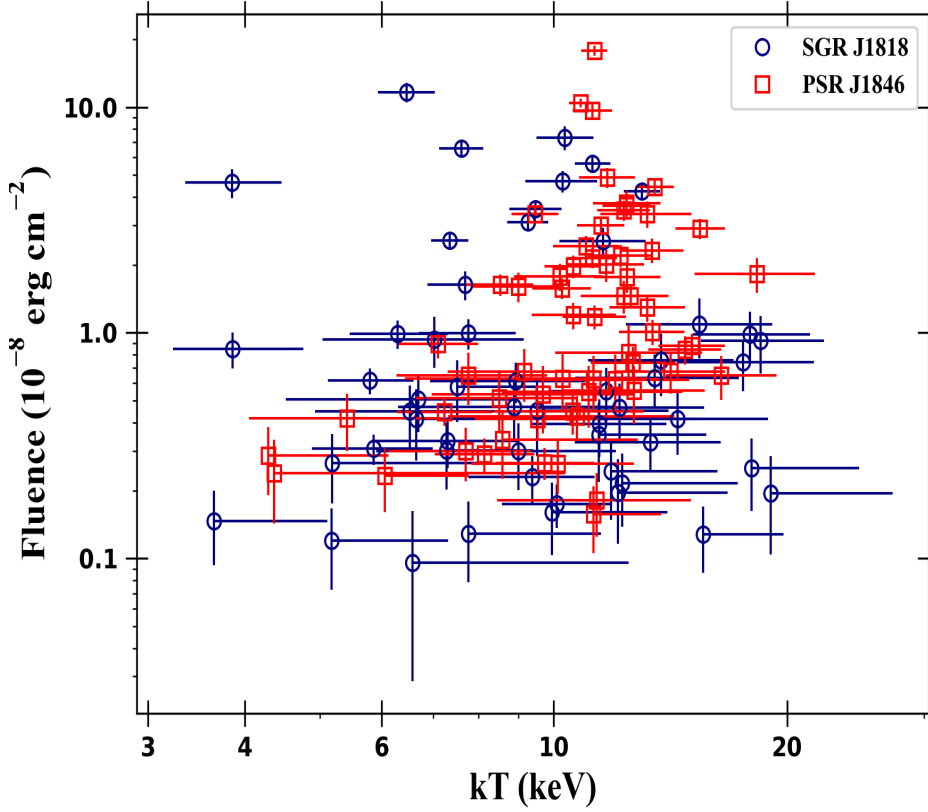


Figure 5.3 Fluence as a function of kT for both *Swift* J1818.0-1607 and PSR J1846.4-0258 events.

In Figure 5.4, we present the cumulative fluence as a function of time. We performed linear fit for the cumulative fluence in different time segments to show the burst energy injection of *Swift* J1818.0-1607 and PSR J1846.4-0258. We used data in 0–52, 53–82, 88–145, and 312–315 day intervals for *Swift* J1818.0-1607, and 0–11, 11–12, and 14–83 day intervals for PSR J1846.4-0258. We calculated the slope of each linear fit as $(1.7 \pm 0.1) \times 10^{-14}$, $(0.7 \pm 0.5) \times 10^{-14}$, $(2.4 \pm 0.2) \times 10^{-14}$, and $(63.3 \pm 8.8) \times 10^{-14} \text{ erg cm}^{-2} \text{ s}^{-1}$ for *Swift* J1818.0-1607, and as $(1.9 \pm 0.2) \times 10^{-14}$, $(2100 \pm 19) \times 10^{-14}$, and $(2.5 \pm 0.2) \times 10^{-14}$ for PSR J1846.4-0258, respectively. Number of data points in the last two time segments of *Swift* J1818.0-1607 events are too few, which causes statistically insignificant slopes. Therefore, we did not fit those segments. We find that PSR J1846.4-0258 showed a rapid rise with an almost vertical trend in cumulative fluence on July 18, 2020, then slowed down the number of emitting bursts per day and cumulative fluence started to follow a linear trend. Moreover, *Swift* J1818.0-1607 emitted more isolated bursts spread over a year without any major clustering.

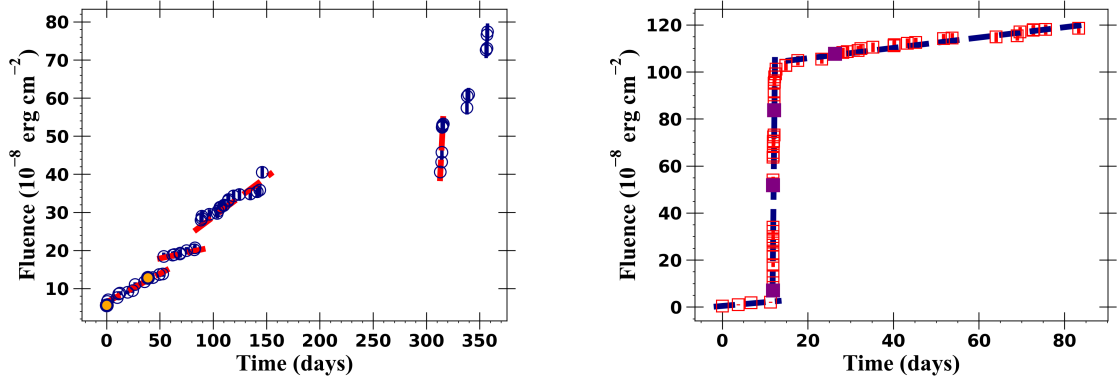


Figure 5.4 Burst cumulative fluence as a function of time for both *Swift* J1818.0-1607 (left) and PSR J1846.4-0258 (right). The first burst observed for both sources are selected as the reference time. Filled data points with orange and purple color represent the triggered events. Red dashed lines represents the least-square linear fits in different time range.

We also calculated the area of the burst emitting region using our single BB-fit parameters, using Stefan-Boltzmann law:

$$(5.1) \quad R^2 = \frac{L}{4\pi\sigma T^4} = \frac{FD^2}{\sigma T^4},$$

where R is the emission area, L is the luminosity, T is the temperature, F is observed flux, and D is the distance to the source. Here, we assume the source distance of 4.8 kpc (Karuppusamy et al., 2020) for *Swift* J1818.0-1607 and 6.0 kpc (Leahy & Tian, 2008) for PSR J1846.4-0258. In Figure 5.5, emitting area (R^2) as a function of kT for all bursts is presented.

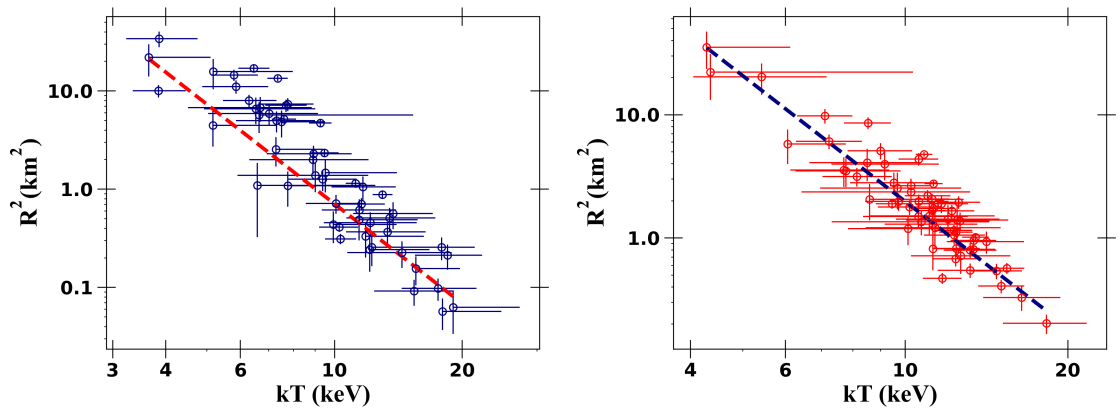


Figure 5.5 Emission areas vs. single BB temperatures for *Swift* J1818.0-1607 (left) and PSR J1846.4-0258 (right).

Both *Swift* J1818.0-1607 and PSR J1846.4-0258 follows similar power law type trend. When we fit our results with power law, we found $R^2 \propto (kT)^{-3.37 \pm 0.33}$ for

Swift J1818.0-1607 and $R^2 \propto (kT)^{-3.39 \pm 0.33}$ for PSR J1846.4-0258, which are similar to the Stefan-Boltzmann law (see the Equation 5.1). Lower energetic single BB corresponds to higher emission area. R^2 values for low kT bursts goes up to ~ 34 km² for *Swift* J1818.0-1607 and ~ 35 km² for PSR J1846.4-0258, which indicates a large area of black body emitting region.

We calculated the correlation factor between R^2 and kT as $\rho = -0.92$ ($p = 8.05 \times 10^{-23}$) for *Swift* J1818.0-1607 and $\rho = -0.87$ ($p = 1.21 \times 10^{-17}$) for PSR J1846.4-0258. The negative correlation factor is consistent with the literature (e.g. $\rho = -0.8$ was reported for SGR J1935+2154 bursts on 2020 excluding the burst-crowded episode (Lin et al., 2020), and $\rho = -0.79$ was reported for the burst crowded episode (Kaneko et al., 2021)).

All 115 bursts that we identified as originated from *Swift* J1818.0-1607 and PSR J1846.4-0258 can be modeled with single BB model. We calculated the weighted average of kT as 7.88 ± 0.15 and 10.71 ± 0.14 keV for *Swift* J1818.0-1607 and PSR J1846.4-0258, respectively. These kT values are comparable to the other magnetars. For example, weighted averages of kT_{low} from BB+BB fits for two different segments were reported as 8.0 ± 0.5 and 7.8 ± 0.3 keV, remaining constant throughout the bursting episode, for the burst crowded episode of SGR J1935+2154 bursts on 2020 (Kaneko et al., 2021)). Figure 5.6 shows BB temperature as histogram, and Figure 5.7 shows BB temperatures as function of time.

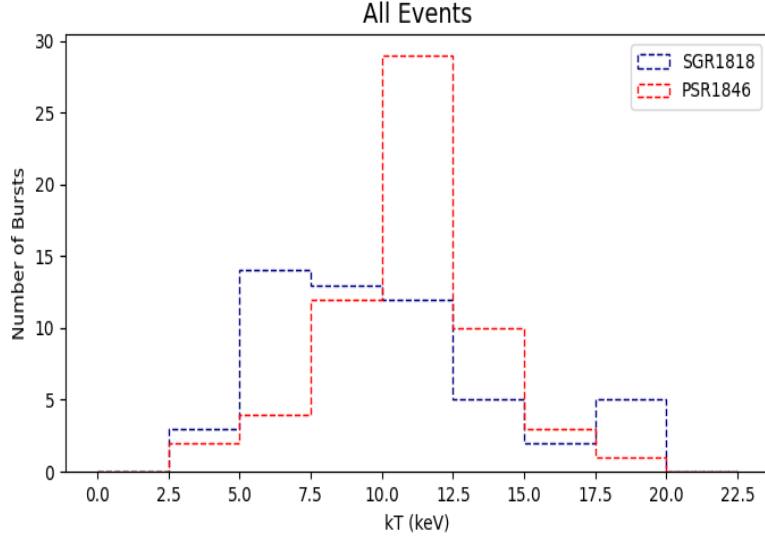


Figure 5.6 Histogram of BB temperature of *Swift* J1818.0-1607 and PSR J1846.4-0258 events.

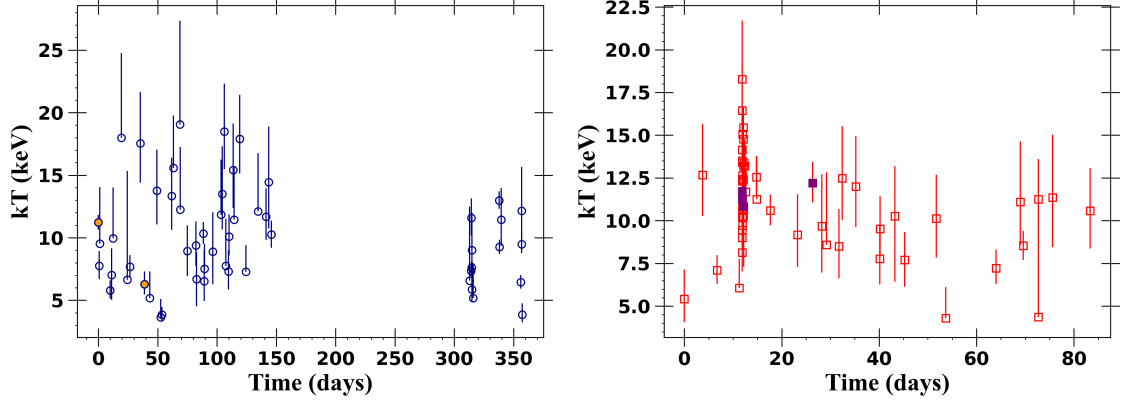


Figure 5.7 BB temperature as a function of time of *Swift* J1818.0-1607 (left) and PSR J1846.4-0258 events (right). Filled data points with orange and purple color represent the triggered events.

In Figure 5.7, we plotted the time evolution of single BB kT for both *Swift* J1818.0-1607 and PSR J1846.4-0258. We found that there is no correlation between kT and time ($\rho = -0.001$ and probability of $p = 0.996$ for *Swift* J1818.0-1607, and $\rho = 0.263$, $p = 0.040$ for PSR J1846.4-0258.). Moreover, we also look at the relation between fluence and single BB kT (see Figure 5.3); however, we could not determine any strong relation between kT and fluence ($\rho = -0.014$ and probability of $p = 0.920$ for *Swift* J1818.0-1607, and $\rho = 0.467$, $p = 0.0001$ for PSR J1846.4-0258.).

5.1 Future Prospects

In this thesis, we searched for untriggered bursts from *Swift* J1818.0-1607 and PSR J1846.4-0258 on 2020 and early 2021 by using our identification method. We completed untriggered burst identification for only two sources, and we used about one year data only. However, identification and spectral investigation of more untriggered SGR bursts are necessary to understand evolution of individual sources and also to improve the magnetar theory. Therefore, we will continue to search untriggered bursts inside other time periods for other SGRs.

Our identification method tries to compensate the poor source localization capabilities of Fermi/GBM by using the positive correlation between count rates and cosine of the detector-to-source angle. For this thesis purposes, we designed the identification code to find only SGR bursts. Our another future goal is to improve our code to find also non-SGR type of untriggered bursts using on our identification method.

BIBLIOGRAPHY

- Ambrosi, E., Barthelmy, S. D., D’Elia, V., Gropp, J. D., Kennea, J. A., Klingler, N. J., Lien, A. Y., Page, K. L., & Neil Gehrels Swift Observatory Team (2020). Trigger 968731: Swift detection of SGR1806-20. GRB Coordinates Network, 27672, 1.
- Archibald, A. M., Kaspi, V. M., Livingstone, M. A., & McLaughlin, M. A. (2008). No Detectable Radio Emission from the Magnetar-Like Pulsar in Kes 75. , 688(1), 550–554.
- Barthelmy, S. D., Gropp, J. D., Kennea, J. A., Kuin, N. P. M., Laha, S., Marshall, F. E., Moss, M. J., Page, K. L., Palmer, D. M., Sbarufatti, B., Siegel, M. H., Tohuvavohu, A., & Neil Gehrels Swift Observatory Team (2020). Swift Detection of a burst from SGR Swift J1818.0-1607. GRB Coordinates Network, 27696, 1.
- Berger, E. (2014). Short-Duration Gamma-Ray Bursts. , 52, 43–105.
- Bernardini, M. G., D’Avanzo, P., Klingler, N. J., Lien, A. Y., Melandri, A., Page, K. L., Palmer, D. M., Sbarrato, T., & Neil Gehrels Swift Observatory Team (2020). Trigger 980513: Swift detection of SGR Swift J1818.0-1607. GRB Coordinates Network, 28055, 1.
- Bissaldi, E., von Kienlin, A., Lichti, G., Steinle, H., Bhat, P. N., Briggs, M. S., Fishman, G. J., Hoover, A. S., Kippen, R. M., Krumrey, M., Gerlach, M., Connaughton, V., Diehl, R., Greiner, J., van der Horst, A. J., Kouveliotou, C., McBreen, S., Meegan, C. A., Paciesas, W. S., Preece, R. D., & Wilson-Hodge, C. A. (2009). Ground-based calibration and characterization of the Fermi gamma-ray burst monitor detectors. Experimental Astronomy, 24(1-3), 47–88.
- Blumer, H., Safi-Harb, S., McLaughlin, M. A., & Fiore, W. (2021). Reactivation of the High Magnetic Field Pulsar PSR J1846-0258 with Magnetar-like Bursts. , 911(1), L6.
- Briggs, M. S. (1996). Low-energy spectral features in GRBs. In Kouveliotou, C., Briggs, M. F., & Fishman, G. J. (Eds.), Gamma-ray Bursts: 3rd Huntsville Symposium, volume 384 of American Institute of Physics Conference Series, (pp. 133–142).
- Camilo, F., Ransom, S. M., Halpern, J. P., Reynolds, J., Helfand, D. J., Zimmerman, N., & Sarkissian, J. (2006). Transient pulsed radio emission from a magnetar. , 442(7105), 892–895.
- Cash, W. (1979). Parameter estimation in astronomy through application of the likelihood ratio. , 228, 939–947.
- Champion, D., Cognard, I., Cruces, M., Desvignes, G., Jankowski, F., Karuppusamy, R., Keith, M. J., Kouveliotou, C., Kramer, M., Liu, K., Lyne, A. G., Mickaliger, M. B., O’Connor, B., Parthasarathy, A., Porayko, N., Rajwade, K., Stappers, B. W., Torne, P., van der Horst, A. J., & Weltevrede, P. (2020). High-cadence observations and variable spin behaviour of magnetar Swift J1818.0-1607 after its outburst. , 498(4), 6044–6056.
- Duncan, R. C. & Thompson, C. (1994). Astrophysics of Very Strongly Magnetized Neutron Stars: A Model for the Soft Gamma Repeaters. In Fishman,

- G. J. (Ed.), *Gamma-Ray Bursts*, volume 307 of *American Institute of Physics Conference Series*, (pp. 625).
- Enoto, T., Sakamoto, T., Younes, G., Hu, C.-P., Ho, W. C. G., Gendreau, K., Arzoumanian, Z., Guver, T., Guillot, S., Altamirano, D., Ray, P. S., Ng, M., Chakrabarty, D., Jaisawal, G. K., & Bogdanov, S. (2020). NICER detection of 1.36 sec periodicity from a new magnetar, Swift J1818.0-1607. *The Astronomer's Telegram*, 13551, 1.
- Esposito, P., Burgay, M., Possenti, A., Turolla, R., Zane, S., de Luca, A., Tiengo, A., Israel, G. L., Mattana, F., Mereghetti, S., Bailes, M., Romano, P., Götz, D., & Rea, N. (2009). Spin-down rate and inferred dipole magnetic field of the soft gamma-ray repeater SGR1627-41. , 399(1), L44–L48.
- Evans, P. A., Gropp, J. D., Kennea, J. A., Klingler, N. J., Laha, S., Lien, A. Y., Page, K. L., Sakamoto, T., & Thovavohu, A. (2020). Swift-BAT trigger 960986: Swift detection of a new SGR Swift J1818.0-1607. *GRB Coordinates Network*, 27373, 1.
- Gamma-ray astronomy Group, U. o. A. H. (2014). rmfit: Forward-folding spectral analysis software. *Astrophysics Source Code Library*, record ascl:1409.011.
- Gavriil, F. P., Gonzalez, M. E., Gotthelf, E. V., Kaspi, V. M., Livingstone, M. A., & Woods, P. M. (2008). Magnetar-Like Emission from the Young Pulsar in Kes 75. *Science*, 319(5871), 1802.
- Goldstein, A., Hamburg, R., Wood, J., Hui, C. M., Cleveland, W. H., Kocevski, D., Littenberg, T., Burns, E., Dal Canton, T., Veres, P., Mailyan, B., Malacaria, C., Briggs, M. S., & Wilson-Hodge, C. A. (2019). Updates to the Fermi GBM Targeted Sub-threshold Search in Preparation for the Third Observing Run of LIGO/Virgo. *arXiv e-prints*, arXiv:1903.12597.
- Gotthelf, E. (2000). Discovery of Young X-Ray Pulsars in the Cores of Supernova Remnants. Presented at the KITP Program: Spin and Magnetism in Young Neutron Stars, Oct 12, 2000, Kavli Institute for Theoretical Physics, University of California, Santa Barbara, id.15.
- Gregory, P. C. & Fahlman, G. G. (1980). An extraordinary new celestial X-ray source. , 287(5785), 805–806.
- Gronwall, C., Gropp, J. D., Kennea, J. A., Laha, S., Lien, A. Y., Marshall, F. E., Page, K. L., Palmer, D. M., & Neil Gehrels Swift Observatory Team (2020). Swift Detection of a burst from SGR Swift J1818.0-1607. *GRB Coordinates Network*, 27746, 1.
- Kaneko, Y. (2005). *Spectral studies of gamma-ray burst prompt emission*. PhD thesis, University of Alabama, Huntsville.
- Kaneko, Y., Göğüş, E., Baring, M. G., Kouveliotou, C., Lin, L., Roberts, O. J., van der Horst, A. J., Younes, G., Keskin, Ö., & Çoban, Ö. F. (2021). Fermi/GBM Observations of the SGRJ1935+2154 Burst Forest. , 916(1), L7.
- Karuppusamy, R., Desvignes, G., Kramer, M., Porayko, N., Champion, D., Torne, P., Stappers, B., van der Horst, A., Kouveliotou, C., & O'Connor, B. (2020). Detection of pulsed radio emission from new magnetar Swift J1818.0-1607. *The Astronomer's Telegram*, 13553, 1.
- Kaspi, V. M. & Beloborodov, A. M. (2017). Magnetars. , 55(1), 261–301.
- Kocevski, D., Burns, E., Goldstein, A., Dal Canton, T., Briggs, M. S., Blackburn, L., Veres, P., Hui, C. M., Hamburg, R., Roberts, O. J., Wilson-Hodge, C. A., Connaughton, V., Racusin, J., Littenberg, T., von Kienlin, A., & Bissaldi, E.

- (2018). Analysis of Sub-threshold Short Gamma-Ray Bursts in Fermi GBM Data. , 862(2), 152.
- Kouveliotou, C., Fishman, G. J., Meegan, C. A., Paciesas, W. S., Wilson, R. B., van Paradijs, J., Preece, R. D., Briggs, M. S., Pendleton, G. N., & Brock, M. N. (1993). Recurrent burst activity from the soft γ -ray repeater SGR 1900+14. , 362(6422), 728–730.
- Krimm, H. A., Lien, A. Y., Page, K. L., Palmer, D. M., Tohuvavohu, A., & Neil Gehrels Swift Observatory Team (2020). Swift Detection of an SGR-like flare from AX J1846.4-0258. GRB Coordinates Network, 28187, 1.
- Leahy, D. A. & Tian, W. W. (2008). The distance of the SNR Kes 75 and PWN PSR J1846-0258 system. , 480(2), L25–L28.
- Liddle, A. R. (2007). Information criteria for astrophysical model selection. , 377(1), L74–L78.
- Lin, L., Göğüş, E., Roberts, O. J., Baring, M. G., Kouveliotou, C., Kaneko, Y., van der Horst, A. J., & Younes, G. (2020). Fermi/GBM View of the 2019 and 2020 Burst Active Episodes of SGR J1935+2154. , 902(2), L43.
- Lin, L., Göğüş, E., Roberts, O. J., Kouveliotou, C., Kaneko, Y., van der Horst, A. J., & Younes, G. (2020). Burst Properties of the Most Recurring Transient Magnetar SGR J1935+2154. , 893(2), 156.
- Livingstone, M. A., Kaspi, V. M., Gotthelf, E. V., & Kuiper, L. (2006). A Braking Index for the Young, High Magnetic Field, Rotation-Powered Pulsar in Kesteven 75. , 647(2), 1286–1292.
- Malacaria, C. & Fermi GBM Team (2020). Fermi GBM observation of a flare from the magnetar SGR 1806-20. GRB Coordinates Network, 27674, 1.
- Mazets, E. P., Golentskii, S. V., Ilinskii, V. N., Aptekar, R. L., & Guryan, I. A. (1979). Observations of a flaring X-ray pulsar in Dorado. , 282(5739), 587–589.
- Meegan, C., Lichti, G., Bhat, P. N., Bissaldi, E., Briggs, M. S., Connaughton, V., Diehl, R., Fishman, G., Greiner, J., Hoover, A. S., van der Horst, A. J., von Kienlin, A., Kippen, R. M., Kouveliotou, C., McBreen, S., Paciesas, W. S., Preece, R., Steinle, H., Wallace, M. S., Wilson, R. B., & Wilson-Hodge, C. (2009). The Fermi Gamma-ray Burst Monitor. , 702(1), 791–804.
- Olausen, S. A. & Kaspi, V. M. (2014). The McGill Magnetar Catalog. , 212(1), 6.
- Rajwade, K., Stappers, B., Lyne, A., Mickaliger, M. B., Preston, L. L., Keith, M., Weltevrede, P., Kramer, M., van der Horst, A., Kouveliotou, C., & O’Connor, B. (2020). Confirmation of pulsed radio emission from Swift J1818.0-1607. The Astronomer’s Telegram, 13554, 1.
- Rajwade, K. M., Stappers, B. W., Lyne, A. G., Shaw, B., Mickaliger, M. B., Liu, K., Kramer, M., Desvignes, G., Karuppusamy, R., Enoto, T., Güver, T., Hu, C.-P., & Surnis, M. P. (2022). Long term radio and X-ray evolution of the magnetar Swift J1818.0-1607. , 512(2), 1687–1695.
- Rea, N. & Esposito, P. (2011). Magnetar outbursts: an observational review. In High-Energy Emission from Pulsars and their Systems, volume 21 of Astrophysics and Space Science Proceedings, (pp. 247).
- Scargle, J. D., Norris, J. P., Jackson, B., & Chiang, J. (2013). The Bayesian Block Algorithm. arXiv e-prints, arXiv:1304.2818.
- Schwarz, G. (1978). Estimating the Dimension of a Model. Annals of Statistics, 6(2), 461–464.
- Tendulkar, S. P., Cameron, P. B., & Kulkarni, S. R. (2013). Proper Motions and

- Origins of AXP 1E 2259+586 and AXP 4U 0142+61. , 772(1), 31.
- Thompson, C. & Duncan, R. C. (1995). The soft gamma repeaters as very strongly magnetized neutron stars - I. Radiative mechanism for outbursts. , 275(2), 255–300.
- Thompson, C. & Duncan, R. C. (2001). The Giant Flare of 1998 August 27 from SGR 1900+14. II. Radiative Mechanism and Physical Constraints on the Source. , 561(2), 980–1005.
- Thompson, C., Lyutikov, M., & Kulkarni, S. R. (2002). Electrodynamics of Magnetars: Implications for the Persistent X-Ray Emission and Spin-down of the Soft Gamma Repeater and Anomalous X-Ray Pulsars. , 574(1), 332–355.
- Turolla, R., Zane, S., & Watts, A. L. (2015). Magnetars: the physics behind observations. A review. Reports on Progress in Physics, 78(11), 116901.
- van der Horst, A. J., Kouveliotou, C., Gorgone, N. M., Kaneko, Y., Baring, M. G., Guiriec, S., Göğüş, E., Granot, J., Watts, A. L., Lin, L., Bhat, P. N., Bissaldi, E., Chaplin, V. L., Finger, M. H., Gehrels, N., Gibby, M. H., Giles, M. M., Goldstein, A., Gruber, D., Harding, A. K., Kaper, L., von Kienlin, A., van der Klis, M., McBreen, S., Mcenery, J., Meegan, C. A., Paciesas, W. S., Pe’er, A., Preece, R. D., Ramirez-Ruiz, E., Rau, A., Wachter, S., Wilson-Hodge, C., Woods, P. M., & Wijers, R. A. M. J. (2012). SGR J1550-5418 Bursts Detected with the Fermi Gamma-Ray Burst Monitor during its Most Prolific Activity. , 749(2), 122.
- van Paradijs, J., Taam, R. E., & van den Heuvel, E. P. J. (1995). On the nature of the ‘anomalous’ 6-s X-ray pulsars. , 299, L41.
- Vidaña, I. (2018). A short walk through the physics of neutron stars. European Physical Journal Plus, 133(10), 445.
- von Kienlin, A., Gruber, D., Kouveliotou, C., Granot, J., Baring, M. G., Göğüş, E., Huppenkothen, D., Kaneko, Y., Lin, L., Watts, A. L., Bhat, N. P., Guiriec, S., van der Horst, A. J., Bissaldi, E., Greiner, J., Meegan, C. A., Paciesas, W. S., Preece, R. D., & Rau, A. (2012). Detection of Spectral Evolution in the Bursts Emitted during the 2008-2009 Active Episode of SGR J1550-5418. , 755(2), 150.
- Zavlin, V. E. & Pavlov, G. G. (2002). Modeling Neutron Star Atmospheres. In Becker, W., Lesch, H., & Trümper, J. (Eds.), Neutron Stars, Pulsars, and Supernova Remnants, (pp. 263).